IEEE Access
Multidisciplinary | Rapid Review | Open Access Journal

Date of publication xxxx 00, 0000, date of current version xxxx 00, 0000.

Digital Object Identifier 10.1109/ACCESS.2021.Doi Number

Modeling and analysis of the stiffness distribution of host–parasite robots

WEI WEI[1,2], GANWEI CAI[2],JUNJIE GONG[2], and SIXU PENG[2]

[1]School of Mechanical and Automotive Engineering,South China University of Technology,Guangzhou, 510641 China
[2]School of Mechanical Engineering, Guangxi University, Nanning, 530004 China

Corresponding author: Ganwei Cai (e-mail: caiganwei@163.com).

This work was supported by the National Natural Science Foundation of China (51765005) ,Guangxi Natural Science Foundation(2018JJB160062) ,and Guangxi Science and Technology Major Projects (Gui Ke AA19254021).

ABSTRACT The stiffness distribution (SD) of robot has a great influence on the robot pose accuracy, but the calculation efficiency and accuracy of stiffness distribution are still low.This study presents a finite element fitting method with an extremely small number of computational cells. It was developed based on experimental results of robot stiffness. This method can be employed to establish single- and multi-source fitted SD (FSD) (S-FSD and M-FSD) models for host–parasite (H–P) robots. The computational efficiency and correctness of the FSD models were verified by case studies.The configurations of six evolutionary mechanisms of an H–P robot were subjected to an SD analysis. A comparison of the six configurations shows that adding parasitic branched chains can improve the SD of the H–P robot to varying degrees. In particular, the most notable improvement was for H–P mechanism. Specifically, by averaging the stiffness of all positions, the average-stiffnesses of H–P mechanism in the *x*-, *y*-, and *z*-directions were 104.10%, 1427.78%, and 1101.62% of those of the host mechanism, respectively. In the SD diagram, the medium- and high-stiffness regions of mechanism F are large and distributed in a banded pattern between the highest pose point and the furthest pose point, whereas its low-stiffness region is small and concentrated near the nearest pose point .

INDEX TERMS Finite element method, fitting method,host–parasite mechanism, robot, stiffness.

I. INTRODUCTION

The different working loads applied to the end of a robot arm are the primary external loads to which the robot is subjected and have the most significant and direct impact on its working accuracy. The stiffness of a robot reflects the mapping relationship between the deformation of its end and the external load and is an important factor that determines its position accuracy. For a robot, a high stiffness suggests that it has a high resistance to deformation caused by external loading and a high working accuracy. Portman devised new stiffness performance indices and used the minimal collinear stiffness value to evaluate the stiffness of mechanisms and robots.[1] Industrial robots, which are primarily serial mechanisms, are extensively used for material handling, spraying, welding, and assembling.[2] The research on the motion error and positioning accuracy of robot has attracted much attention.[3-5]Compared to numerically controlled machine tools, industrial robotic manipulators have a relatively low stiffness due to their cantilever position. The stiffness of a large industrial robot is generally lower than 1 N/μm, whereas the stiffness of a numerically controlled machine tool is usually greater than 50N/μm.[6] Liu et al.[7] proposed a new passive, power-source-free, stiffness-self-adjustable mechanism. Orekhov and Simman[8] examined the use of a combination of kinematic redundancy and variable-stiffness actuators to adjust stiffness in real time. Chen et al.[9] investigated the negative active stiffness produced by a redundantly actuated planar rotational parallel mechanism. Jin et al.[10] presented an optimal design of a redundantly actuated symmetrical parallel mechanism with five revolute joints developed based on structural stiffness. Li et al.[11] formulated a design method to prevent negative stiffness in redundant planar rotational parallel mechanisms. Manifestly, improving the stiffness of a mechanism is vitally important for enhancing its performance.

The stiffness distribution (SD) of a robot refers to the distribution of the stiffnesses of the end of its arm in all the poses within its working space. The joints of robot considered rigid and no clearance in the joint.The SD is a theoretical basis for the structural design and optimization of a robot.[12] Wu et al.[13] studied the stiffness of a hybrid

This article has been accepted for publication in a future issue of this journal, but has not been fully edited. Content may change prior to final publication. Citation information: DOI 10.1109/ACCESS.2021.3063296, IEEE Access

machine tool with five degrees of freedom (DOFs) and actuation redundancy and established an accurate stiffness model for the machine tool using the assembly method after deriving stiffness matrices for all the components of the machine tool. Huang and Schimmels[14] performed an eigenscrew decomposition of spatial stiffness matrices. Wu[15] analyzed and optimized the stiffness of a coaxial spherical parallel manipulator. Li et al.[16] analyzed a soft robotic fish with variable-stiffness decoupled mechanisms. He et al.[17] proposed a new general stiffness model, which includes linear and nonlinear stiffness models, for serial mechanisms. Yu et al.[18] calculated and analyzed the dynamic stiffness of a symmetrical crank slider mechanism with a variable-stiffness joint. Lu et al.[19] suggested a new method for calculating the stiffness of bolted connectors and analyzed the effects of joint surface stiffness on the overall stiffness. Liu et al.[20] developed an exact dynamic stiffness method for multi-body systems composed of beams and rigid bodies.There are two main types of robot stiffness modeling, namely, finite element (FE)[21] and analytical[22] methods. FE methods can describe aspects, such as the structural geometric dimensions, physical material properties, contact conditions, and load distribution, of robots in a comprehensive and detailed manner. However, when the pose of a mechanism changes, it is necessary to reimport its geometric model, regenerate a mesh, and set the contact parameters and external loading. Modeling complex configurations is computationally expensive in terms of time. In contrast, analytical methods are characterized by their high computational speed. However, analytical methods are unable to reflect the actual stiffness of a mechanism comprehensively and accurately due to their simplifications.

The host-parasite (H-P) phenomenon is ubiquitous in both the plant and animal kingdoms.[23, 24] Inspired by the parasitism between trees and rattans, Wei et al.[25] proposed an H-P structure that can characterize the hierarchical relationships between the DOFs of the sub-mechanisms of a mechanism. The local DOFs are modeled as H-P relationships like those in the biological world. A new industrial H-P robot, developed by Wei et al.,[25] is able to reach gravitational equilibrium and had notably improved stiffness.

In summary, there has been measurable and valuable progress in the FE and analytical methods used for modeling robot stiffness. However, there are deficiencies in FE (e.g., long computational times) and analytical (e.g., oversimplification) methods. The external loads to which a robot is subjected consist primarily of the various working loads on the end of its arm. To analyze the effects of adding different parasitic branched chains on the SD of an H-P robot, this study presents an FE fitting method that uses an extremely small number of mesh cells in modeling. An attempt was made to calculate SD patterns efficiently and accurately for different evolutionary configurations of an H–P robot using SD modeling through multiple fitting operations for multiple poses. The configurations of six evolutionary mechanisms of an H–P robot were subjected to an SD analysis.Analyzing the SD of a robot not only can determine its high-stiffness working regions, which can be used for tasks with relatively high accuracy requirements, but can also provide a foundation for the structural design and optimization of new robots.For example,a design of flexible joint robot manipulator or PAM(Pneumatic Artificial Muscle) actuated manipulator.

II. STRUCTURAL AND KINEMATIC ANALYSIS OF H-P ROBOTS

A. STRUCTURE AND DOF DISTRIBUTION OF H-P ROBOTS

Hybrid mechanisms that are composed of host and parasitic mechanisms and display H–P relationships are referred to as H–P mechanisms.[25] An H–P relationship includes two types of precedence relationship, namely, one in which a host mechanism precedes the parasitic mechanisms and one in which the parasitic branched chains of a previous level precede those of a secondary level. For an H–P mechanism that satisfies such an H–P relationship, its internal host and parasitic mechanisms can be divided in multiple ways. Wei et al.[25] proposed a new H–P palletizing robot. Figure 1 shows a three-dimensional (3D) diagram of this robot and a photograph of a prototype.[25] Based on the differences in geometric dimensions as well as real-world motion and stress conditions, the composition of the branched chains of the host and parasitic mechanisms of this H–P robot was adjusted in this study.

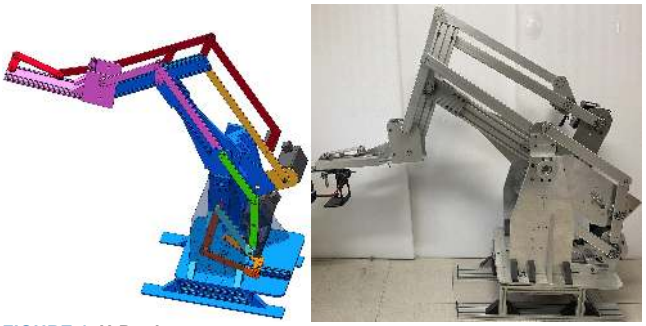

FIGURE 1. H-P robot.

The new H–P robot consists of one host branched chain (i.e., branched chain A) and six parasitic branched chains (i.e., branched chains B–G). Figure 2 is a structural diagram of this robot. The branched chain of the host mechanism has multiple components that have a relatively large geometrical cross-sectional area. It has independent DOFs, plays a major load-bearing role, and is subject to axial and shear forces, bending moments, and torques. The six parasitic branched chains have links with a relatively small geometric cross-sectional area. They each have no independent DOFs and rely on the host branched chain or the parasitic branched chain of the previous level to exist and play a driving role. The links comprising the parasitic branched chains are subject primarily to axial forces and bending moments.

This article has been accepted for publication in a future issue of this journal, but has not been fully edited. Content may change prior to final publication. Citation information: DOI 10.1109/ACCESS.2021.3063296, IEEE Access

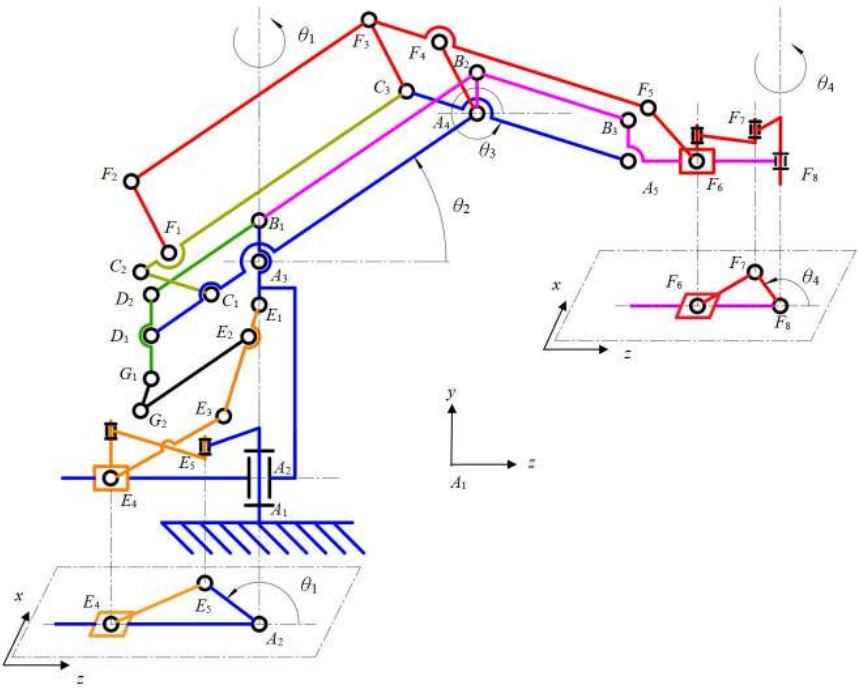

FIGURE 2. Structural diagram of the new H-P robot.

Wei et al.[25] detailed a method for calculating the number of DOFs of a H–P mechanism. The total number of DOFs of a H–P mechanism is given by:

$$F_{HP} = F_H + \sum F_P \tag{1}$$

where F_H and F_P are the numbers of DOFs for the host and parasitic mechanisms, respectively.

The number of DOFs of the host mechanism is given by:

$$F_H = 6(n_H - g_H - 1) + \sum f_H + \mu_H \tag{2}$$

where n_H is the number of components, g_H is the number of motion joints, $f_{H,j}$ is the number of DOFs of the jth motion joint, and μ_H is the number of overconstraints of the mechanism, which consists of the number of general constraints λ_H and the number of redundant constraints (i.e., virtual constraints) v_H:

$$\mu_H = v_H - \lambda_H \left(n_H - g_H - 1\right) \tag{3}$$

The number of DOFs of a parasitic mechanism is given by:

$$\begin{aligned} F_P &= 6(n_P + 1 - g_P - 1) + \sum f_P + \mu_P \\ &= 6(n_P - g_P) + \sum f_P + \mu_P \end{aligned} \tag{4}$$

and

$$\mu_P = v_P - \lambda_P \left(n_P + 1 - g_P - 1\right) = v_P - \lambda_P \left(n_P - g_P\right) \tag{5}$$

where n_P is the number of components, g_P the number of motion joints, $f_{P,j}$ the number of DOFs of the jth motion joint, and μ_P the number of overconstraints of the mechanism, which consists of the number of general constraints λ_P and the number of redundant constraints (i.e., virtual constraints) v_P. In addition, the 1 in the term n_P+1 in the above equations means that the parasitized mechanism is treated as a component. This is the key to correctly calculating the number of DOFs of a parasitic mechanism. A parasitized mechanism is generally the parasitic mechanism of the previous level or the host mechanism.

Table I summarizes the calculation of the numbers of DOFs of different branched chains of an H–P robot. Based on (1), the total number of DOFs of the new H–P robot is as follows:F=3+0+0+0+0+1+0=4 . Let θ_1, θ_2, θ_3, and θ_4, be the drive angles of the four drive motors of the H–P robot, respectively.

TABLE I
NUMBER OF DOFS OF DIFFERENT BRANCHED CHAINS OF AN H-P ROBOT

Chain	Color	n	g	u	v	λ	Equations used for calculation	F_i
A	Blue	4	3	0	0	3	(2) and (3)	3
B	Pink	4	6	6	0	3	(4) and (5)	0
C	Yellow	2	3	3	0	3	(4) and (5)	0
D	Green	2	3	3	0	3	(4) and (5)	0
E	Orange	4	6	6	0	3	(4) and (5)	0
F	Red	9	13	12	0	3	(4) and (5)	1
G	Black	2	3	3	0	3	(4) and (5)	0

B. KINEMATIC MODEL OF THE ROBOT

First, a kinematic model is established for the host branched chain (i.e., branched chain A). The spatial coordinates of each motion joint of branched chain A are as follows:

$$\begin{aligned} x_{0,A_i} &= x_{0,A_{i-1}} + l_{A_i} \cos(\theta_{A_{x,i}}) \\ y_{0,A_i} &= y_{0,A_{i-1}} + l_{A_i} \sin(\theta_{A_{y,i}}) \\ z_{0,A_i} &= z_{0,A_{i-1}} + l_{A_i} \cos(\theta_{A_{z,i}}) \end{aligned} \tag{6}$$

where $x_{0,Ai}$, $y_{0,Ai}$, and$z_{0,Ai}$ are the spatial coordinates of node A_i (0 means that this node belongs to the parasitized branched chain of level 0, i.e., the host branched chain). l_{Ai} is the projected length of the link with A_i as its starting point on the corresponding plane, and $\theta_{Ax,i}$, $\theta_{Ay,i}$, and $\theta_{Az,i}$ are the angles between the projections of the link with A_i as its starting point on the corresponding planes and the coordinate axes. It is possible to establish the functional relationships of $\theta_{Ax,i}$,

This article has been accepted for publication in a future issue of this journal, but has not been fully edited. Content may change prior to final publication. Citation information: DOI 10.1109/ACCESS.2021.3063296, IEEE Access

$\theta_{Ay,i}$, and $\theta_{Az,i}$ with the drive angles based on the geometric relationships.

Next, a kinematic model is established for each parasitic branched chain (i.e., branched chains B–G). The spatial coordinates of each motion joint of a parasitic branched chain are given by:

$$\begin{aligned} x_{j,W_i} &= x_{j-1,W_{i-1}} + l_{W_i}\cos(\theta_{W_{x,i}}) \\ y_{j,W_i} &= y_{j-1,W_{i-1}} + l_{W_i}\sin(\theta_{W_{y,i}}) \\ z_{j,W_i} &= z_{j-1,W_{i-1}} + l_{W_i}\cos(\theta_{W_{z,i}}) \\ W_i &\in [B_i, C_i, D_i, E_i, F_i, G_i,] \end{aligned} \tag{7}$$

where $x_{j,Wi}$, $y_{j,Wi}$, and $z_{j,Wi}$ are the spatial coordinates of node W_i of a certain parasitic branched chain $W \in [B,C,D,E.F,G]$ and j means that this node belongs to the parasitized branched chain of the jth level. Node W_{i-1} is the parasitic joint of the link where node W_i is located and belongs to the parasitized branched chain of the $(j-1)$th level. l_{Wi} is the projected length of the link with W_i as its starting point on the corresponding plane, and $\theta_{Wx,i}$, $\theta_{Wy,i}$, and $\theta_{Wz,i}$ are the angles between the projections of the link with W_i as its starting point on the corresponding planes and the coordinate axes. It is possible to establish the functional relationships of $\theta_{Wx,i}$, $\theta_{Wy,i}$, and $\theta_{Wz,i}$ with the drive angles based on the geometric relationships.

C. WORKING SPACE OF THE ROBOT

The working space of the robot is composed of a combination of all the spatial points that its end can reach and is expressed with vertical and horizontal projections. The working space of the robot on the xz plane (i.e., the horizontal plane) is an annular area. The inner and outer radii of this annular area are the contraction and extension limits of the manipulator, respectively. The range of the angle of rotation of the ring is $\theta_1 \in [300°,420°]$. The position of joint point F_8 at the end of the robot within the xz plane is given by:

$$x_{F_8} = z_{F_8}\cos(\theta_1) \tag{8}$$

Within the yz plane (i.e., the vertical plane), because the host mechanism has independent DOFs but the parasitic mechanisms have no independent DOFs, a position analysis of the robot is equivalent to an analysis of the host mechanism (i.e., the serial mechanism composed of branched chain A and link A_5F_8), as shown in Figure 2. The position of joint point F_8 within the yz plane is given by:

$$y_{F_8} = l_{A_1A_2} + l_{A_2A_3} + l_{A_3A_4}\sin(\theta_2) + l_{A_4A_5}\sin(\theta_3) \tag{9}$$

$$z_{F_8} = l_{A_3A_4}\cos(\theta_2) + l_{A_4A_5}\cos(\theta_3) + l_{A_5F_8} \tag{10}$$

where l_{A1A2}, l_{A2A3}, l_{A3A4}, l_{A4A5}, and l_{A5F8} are the lengths of the links of branched chain A and the end link of branched chain B, respectively (l_{A1A2} = 0.155 m, l_{A2A3} = 0.585 m, l_{A3A4} = 0.776 m, l_{A4A5} = 0.420 m, and l_{A5F8} = 0.622 m), and θ_2 and θ_3 are the working angles of rotation of links A_3A_4 and A_4A_5, respectively.

To avoid interference between the parasitic branched chains as well as singular configurations, the angles of rotation of the manipulator of the H–P robot are limited as follows: $\theta_2 \in [352.51°,397.44°]$, $\theta_3 \in [290.00°,341.97°]$, and θ_2-$\theta_3 \geq 52.17°$. A total of 30,000 robot poses were randomly generated using the Monte Carlo method. Subsequently, the projection of the working space of the robot on the yz plane was calculated, as shown in Figure 3. The working area of the robot is enclosed by four extreme pose points, namely, the highest point P_1 (1.638 m, 1.229 m), the furthest point P_2 (1.7076 m, 0.901 m), the lowest point P_3 (1.538 m, 0.396 m), and the nearest point P_4 (1.384 m, 0.966 m), which correspond to poses P'_{p1}, P'_{p2}, P'_{p3}, and P'_{p4}, respectively.

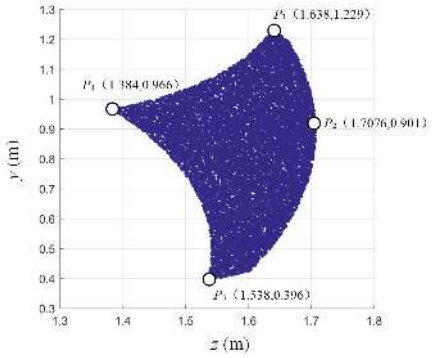

FIGURE 3. Projection of the working space of the robot on the *yz* plane.

III. FITTED SD MODELS OF H–P ROBOTS

A. DIFFERENT FITTED SD MODELS

For the stiffness at a single node (e.g., the output node at the end of a robot) in a single pose, based on the significant results for the deformation of the mechanism under a specific unidirectional external load, comprehensive fitting factors a_A, a_{Iy}, a_{Iz} ,and a_J are introduced for the characteristic boundary conditions (cross-sectional area A, cross-sectional moments of inertia I_y and I_z, and polar moment of inertia J) composing the stiffness matrix of the mechanism. The SD of a robot refers to the distribution of its stiffnesses in all the poses within its working range.

Mechanism stiffness models can be categorized into three types based on the goodness of fit: (1) non-fitted SD (FSD; e.g., an ANSYS Workbench simulation model), (2) single-source FSD (S-FSD), and (3) multi-source FSD (M-FSD) models.

1. ADVANTAGES OF A NON-FSD MODEL

Computer hardware resources permitting, it is possible to obtain a stiffness matrix relatively close to an actual rigid-frame structure through a large number of mesh cells that restore the details of the geometric model. The following is the fitting factor matrix of a non-FSD model:

$$a = [a_A \;\; a_{I_y} \;\; a_{I_z} \;\; a_J]^T = [1 \;\; 1 \;\; 1 \;\; 1]^T \tag{11}$$

The following is the characteristic boundary parameter matrix:

$$\begin{aligned} R &= [a_A A' \;\; a_{I_y} I'_y \;\; a_{I_z} I'_z \;\; a_J J']^T \\ &= [A' \;\; I'_y \;\; I'_z \;\; J']^T \end{aligned} \tag{12}$$

where A' is the cross-sectional area of the element, I'_y is the cross-sectional moment of inertia within the xz coordinate plane, I'_z is the cross-sectional moment of inertia within the

This article has been accepted for publication in a future issue of this journal, but has not been fully edited. Content may change prior to final publication. Citation information: DOI 10.1109/ACCESS.2021.3063296, IEEE Access

xy coordinate plane, and J' is the polar moment of inertia of the element.

2. ADVANTAGES OF AN S-FSD MODEL

Based on the stiffness values calculated by the non-FSD model for single poses, the fitting factors are subjected to a single-source fitting procedure. A fitted stiffness model with an extremely small number of computational cells (i.e., an S-FSD model) is, thus, obtained. The stress-induced deformation calculated by the S-FSD model is basically consistent with that calculated by the non-FSD model, which contains an extremely large number of computational cells. The S-FSD model can accurately calculate the stress-induced deformation of the robot in a single pose under any load and requires significantly less computational time for a single pose.

3. ADVANTAGES OF AN M-FSD MODEL

Following on from the S-FSD model, based on the experimental stiffness measurements for multiple poses as well as the distribution of the DOFs of each branched chain of the mechanism, the link and beam elements are differentiated. Subsequently, the fitting factors are fitted based on the type of element. The results of the analysis of the stress-induced deformation are basically consistent with the experimental stiffness measurements. Finally, an accurate SD that is basically consistent with the actual SD of the physical prototype is obtained.

B. M-FSD MODELING STEPS FOR AN H–P ROBOT

Figure 4 is a flowchart of the M-FSD modeling of an H–P robot. The following details the steps:

Step 1: Determine the objective of analysis, which is to establish an M-FSD model for the H–P robot.

Step 2: Select a single pose of the robot and establish a non-FSD model and a preliminary S-FSD model based on the beam elements.

Step 3: Determine a fitting sequence for the fitting factors (a_A, a_{Iy}, a_{Iz} ,and a_J) based on the preliminary S-FSD model and the significant results for the deformation of the mechanism under unidirectional external loading.

Step 4: Fit the stress-induced deformation in various directions based on the non-FSD model and the fitting sequence determined in Step 3. Determine the fitting factors using the Monte Carlo method. Thus, establish a single-pose S-FSD model.

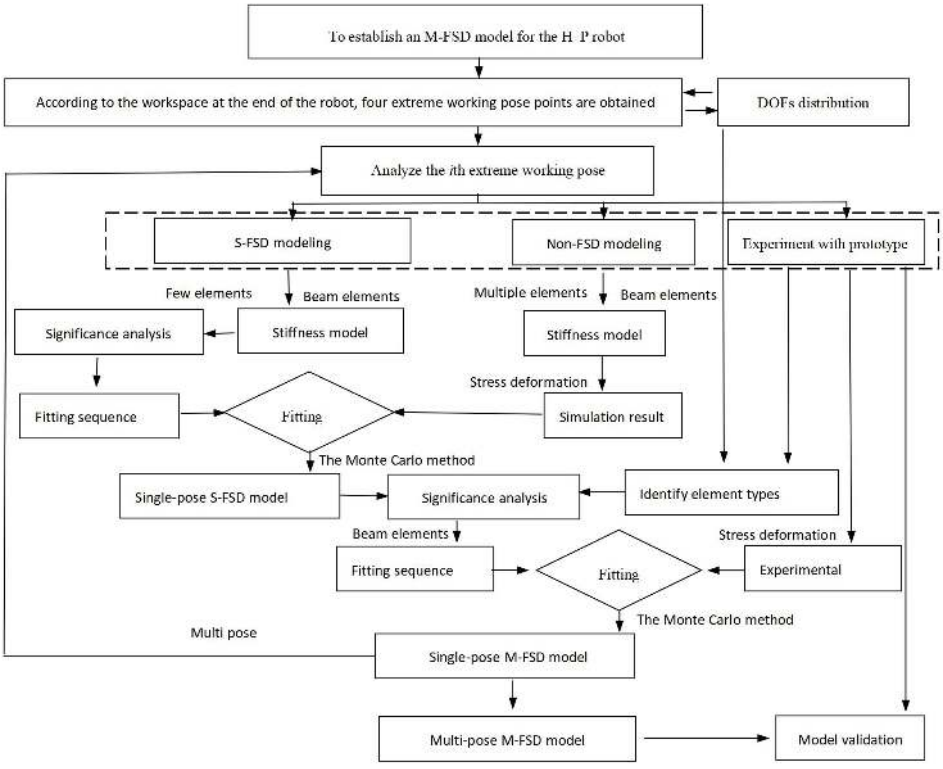

FIGURE 4. Flowchart of the M-FSD modeling of an H–P robot.

Step 5: Differentiate the link and beam elements based on the distribution of the DOFs of each branched chain of the mechanism (the beam elements include the links of the host and parasitic branched chains where the drive motors are mounted, while the other links are categorized as link elements).

Step 6: Perform a significance analysis on the beam elements alone based on the preliminary M-FSD model and determine a fitting sequence for the beam elements. Use fitting factors a_A and a_{Iz} of the S-FSD model for the link elements (for the link elements, because of their very small distortional deformation and bending deformation in the y-

This article has been accepted for publication in a future issue of this journal, but has not been fully edited. Content may change prior to final publication. Citation information: DOI 10.1109/ACCESS.2021.3063296, IEEE Access

direction, their deformation is approximately simplified by a 100-fold reduction, i.e., a_J=100 and a_{Iy}=100).

Step 7: Fit the stress-induced deformation in different directions in succession based on the S-FSD model and the fitting sequence determined in Step 6. Determine the fitting factors using the Monte Carlo method. Thus, establish a single-pose M-FSD model.

Step 8: Select multiple poses of the robot and repeat Steps 2–7 to obtain the corresponding fitting factors for different poses. Establish a multi-pose M-FSD model through a weighted integration of the fitting factors for multiple different poses.

Step 9: Validate the correctness of the multi-pose M-FSD model.

C. STIFFNESS MODEL OF THE NEW H–P ROBOT

Based on its structural diagram in Figure 2, the H–P robot, which is composed of connecting links, can be divided into 36 two-node beam elements. In a local coordinate system for elements, the nodal variables are given by:

$$\delta^e = [u_1 \ v_1 \ w_1 \ \theta_{x1} \ \theta_{y1} \ \theta_{z1} \ u_2 \ v_2 \ w_2 \ \theta_{x2} \ \theta_{y2} \ \theta_{z2}]^T \quad (13)$$

where u_i,v_i,and w_i are the displacements at node i along the local coordinate directions and θ_{xi}, θ_{yi} ,and θ_{zi} are the angles of rotation of the cross section at node i around the three coordinate axes (specifically, θ_{xi} is the angle of rotation of the cross section and θ_{yi} and θ_{zi} are the angles of rotation of the cross section within the xz and xy coordinate planes, respectively).

The nodal forces are given by:

$$F^e = [U_1' \ V_1' \ W_1' \ M_{x1}' \ M_{y1}' \ M_{z1}' \ U_2' \ V_2' \ W_2' \ M_{x2}' \ M_{y2}' \ M_{z2}']^T \quad (14)$$

where U'_i is the axial force at node i and V'_i and W'_i are the shear forces at node i within the xz and xy coordinate planes, respectively, M'_{xi} is the torque at node i, and M'_{yi} and M'_{zi} are the bending moments within the xz and xy coordinate planes, respectively.

For the non-FSD model, the characteristic boundary parameters (A',I'_y,I'_z,J') of its stiffness matrix can be represented by r:

$$r = [A' \ I_y' \ I_z' \ J']^T \quad (15)$$

where A' is the cross-sectional area of the element, I'_y and I'_z are the cross-sectional moments of inertia of the element within the xz and xy coordinate planes, respectively, and J' is the polar moment of inertia of the element.

For the FSD models, fitting factors a_A, a_{Iy}, a_{Iz} , and a_J are introduced for the four characteristic boundary parameters of the stiffness matrix, respectively. These fitting factors can be represented by matrix a:

$$a = [a_A \ a_{I_y} \ a_{I_z} \ a_J]^T \quad (16)$$

The fitted characteristic boundary parameters of the stiffness matrix can be represented by matrix R:

$$\begin{aligned} R &= ra \\ &= [A \ I_y \ I_z \ J]^T \\ &= [a_A A' \ a_{I_y} I_y' \ a_{I_z} I_z' \ a_J J']^T \end{aligned} \quad (17)$$

where A is the fitted cross-sectional area of the element, I_y and I_z are the fitted cross-sectional moments of inertia within the xz and xy coordinate planes, respectively, and J is the fitted polar moment of inertia of the element.

Table II summarizes the characteristics of the characteristic boundary parameters of the three types of model that significantly affect mechanism deformation.

TABLE II
CHARACTERISTICS OF THE CHARACTERISTIC BOUNDARY PARAMETERS OF THE THREE TYPES OF MODEL

	Non-FSD model	S-FSD model	M-FSD model	
Mechanism Element	Mechanism Beam	Mechanism Beam	H–P robot Link	Beam
Source of fitting	Non	Non-FSD model	Non-FSD model	Experiment
Parameter 1	A'	$a_A A'$	$a_A A'$	$a'_A a_A A'$
Parameter 2	J'	$a_J J'$	$a_J J'$,a_J=100	$a'_J a_J J'$
Parameter 3	I'_y , I'_z	$a_{Iy} I'_y$, $a_{Iz} I'_z$	$a_{Iy} I'_y$, $a_{Iz} I'_z$, a_{Iy}=100	$a'_{Iy} a_{Iy} I'_y$ $a'_{Iz} a_{Iz} I'_z$

The following is the stiffness matrix of the elements of the H–P robot mechanism when using Euler–Bernoulli beams:

This article has been accepted for publication in a future issue of this journal, but has not been fully edited. Content may change prior to final publication. Citation information: DOI 10.1109/ACCESS.2021.3063296, IEEE Access

$$K^e=\begin{bmatrix}
\frac{EA}{l} & 0 & 0 & 0 & 0 & 0 & -\frac{EA}{l} & 0 & 0 & 0 & 0 & 0\\
0 & \frac{12EI_z}{l^3} & 0 & 0 & 0 & \frac{6EI_z}{l^2} & 0 & -\frac{12EI_z}{l^3} & 0 & 0 & 0 & \frac{6EI_z}{l^2}\\
0 & 0 & \frac{12EI_y}{l^3} & 0 & -\frac{6EI_y}{l^2} & 0 & 0 & 0 & -\frac{12EI_y}{l^3} & 0 & -\frac{6EI_y}{l^2} & 0\\
0 & 0 & 0 & \frac{GJ}{l} & 0 & 0 & 0 & 0 & 0 & -\frac{GJ}{l} & 0 & 0\\
0 & 0 & -\frac{6EI_y}{l^2} & 0 & \frac{4EI_y}{l} & 0 & 0 & 0 & \frac{6EI_y}{l^2} & 0 & \frac{2EI_y}{l} & 0\\
0 & \frac{6EI_z}{l^2} & 0 & 0 & 0 & \frac{4EI_z}{l} & 0 & -\frac{6EI_z}{l^2} & 0 & 0 & 0 & \frac{2EI_z}{l}\\
-\frac{EA}{l} & 0 & 0 & 0 & 0 & 0 & \frac{EA}{l} & 0 & 0 & 0 & 0 & 0\\
0 & -\frac{12EI_z}{l^3} & 0 & 0 & 0 & -\frac{6EI_z}{l^2} & 0 & \frac{12EI_z}{l^3} & 0 & 0 & 0 & -\frac{6EI_z}{l^2}\\
0 & 0 & -\frac{12EI_y}{l^3} & 0 & \frac{6EI_y}{l^2} & 0 & 0 & 0 & \frac{12EI_y}{l^3} & 0 & \frac{6EI_y}{l^2} & 0\\
0 & \frac{6EI_z}{l^2} & 0 & -\frac{GJ}{l} & 0 & 0 & 0 & 0 & 0 & \frac{GJ}{l} & 0 & 0\\
0 & 0 & -\frac{6EI_y}{l^2} & 0 & \frac{2EI_y}{l} & 0 & 0 & 0 & \frac{6EI_y}{l^2} & 0 & \frac{4EI_y}{l} & 0\\
0 & 0 & 0 & 0 & 0 & \frac{2EI_z}{l} & 0 & -\frac{6EI_z}{l^2} & 0 & 0 & 0 & \frac{4EI_z}{l}
\end{bmatrix} \tag{18}$$

The following is the transformation matrix between the local and global coordinate systems for the elements of the H–P robot mechanism:

$$T=\begin{bmatrix} t & 0 & 0 & 0\\ 0 & t & 0 & 0\\ 0 & 0 & t & 0\\ 0 & 0 & 0 & t \end{bmatrix} \tag{19}$$

where

$$t=\begin{bmatrix} \cos(x,\bar{x}) & \cos(x,\bar{y}) & \cos(x,\bar{z})\\ \cos(y,\bar{x}) & \cos(y,\bar{y}) & \cos(y,\bar{z})\\ \cos(z,\bar{x}) & \cos(z,\bar{y}) & \cos(z,\bar{z}) \end{bmatrix} \tag{20}$$

The first row of submatrix t can be calculated based on the coordinates of the node in the ($\bar{x}$, $\bar{y}$, $\bar{z}$)global coordinate system:

$$\begin{aligned}
\cos(x,\bar{x})&=\frac{\bar{x}_2-\bar{x}_1}{l}\\
\cos(x,\bar{y})&=\frac{\bar{y}_2-\bar{y}_1}{l}\\
\cos(x,\bar{z})&=\frac{\bar{z}_2-\bar{z}_1}{l}\\
l&=\sqrt{(\bar{x}_2-\bar{x}_1)^2+(\bar{y}_2-\bar{y}_1)^2+(\bar{z}_2-\bar{z}_1)^2}
\end{aligned} \tag{21}$$

An auxiliary reference coordinate system (x',y',z') is required to determine the other rows of submatrix t.

The following is the transformation matrix between the (x',y',z') auxiliary reference coordinate system and the ($\bar{x}$, $\bar{y}$, $\bar{z}$) global coordinate system:

$$t_1=\begin{bmatrix} l & m & n\\ -\frac{m}{l} & \frac{l}{\lambda} & 0\\ -\frac{nl}{\lambda} & -\frac{mn}{\lambda} & \lambda \end{bmatrix} \tag{22}$$

Where

$$\begin{aligned}
\cos(x,\bar{x})&=\frac{\bar{x}_j-\bar{x}_i}{L}=l\\
\cos(x,\bar{y})&=\frac{\bar{y}_j-\bar{y}_i}{L}=m\\
\cos(x,\bar{z})&=\frac{\bar{z}_j-\bar{z}_i}{l}=n\\
\lambda&=\sqrt{l^2+m^2}
\end{aligned} \tag{23}$$

and

$$L=\sqrt{(\bar{x}_j-\bar{x}_i)^2+(\bar{y}_j-\bar{y}_i)^2+(\bar{z}_j-\bar{z}_i)^2} \tag{24}$$

The following is the transformation matrix between the (x',y',z') auxiliary reference coordinate system and the (x,y,z) local coordinate system:

$$t_2 = \begin{bmatrix} 1 & 0 & 0 \\ 0 & \cos\alpha & \sin\alpha \\ 0 & -\sin\alpha & \cos\alpha \end{bmatrix} \tag{25}$$

where α is the angle between the y-axis of the local coordinate system and the y'-axis of the auxiliary coordinate system. Submatrix t can be expressed as follows:

$$t = t_2 t_1 = \begin{bmatrix} 1 & 0 & 0 \\ 0 & \cos\alpha & \sin\alpha \\ 0 & -\sin\alpha & \cos\alpha \end{bmatrix} \begin{bmatrix} l & m & n \\ -\frac{m}{l} & \frac{l}{\lambda} & 0 \\ -\frac{nl}{\lambda} & -\frac{mn}{\lambda} & \lambda \end{bmatrix} \tag{26}$$

If the element is perpendicular to the global coordinate system (i.e., the x-axis of the element is parallel to the $\bar{z}$-axis of the global coordinate system), then the transformation matrix is transformed to

$$t_2 = \begin{bmatrix} 0 & 0 & 1 \\ -\sin\alpha & \cos\alpha & 0 \\ -\cos\alpha & -\sin\alpha & 0 \end{bmatrix} \tag{27}$$

Thus, the relationship between the element node displacements in the local and global coordinate systems can be expressed as:

$$\delta^e = T\bar{\delta}^e \tag{28}$$

By substituting (28) into the FE equation and pre-multiplying the equation by , a characteristic element matrix in the global coordinate system is obtained:

$$\bar{K}^e = T^T \bar{K}^e T \tag{29}$$

The force vector is given by:

$$\bar{F}^e = T^T F^e \tag{30}$$

By integrating the element matrix and the vector, a stiffness model is obtained for the H–P robot:

$$K = \frac{F}{\delta} \tag{31}$$

D. SIGNIFICANCE ANALYSIS OF DEFORMATION RESPONSE AND FITTING SEQUENCE

Stiffness matrix K is composed of the characteristic matrices of the axial-force, bending, and torsional elements, which are independent of each another. $a_A A'$ and $a_J J'$ are the characteristic boundary parameters of the axial-force and torsional elements and determine their tensile/compressive deformation and torsional deformation, respectively. $a_{Iy} I'_y$ and $a_{Iz} I'_z$ are the characteristic boundary parameters of the bending elements and determine their bending deformation in two different planes.

Here, the pose of the H–P robot at point P_1 is selected. In addition, a unidirectional load of –50N is applied in succession to the target node along each of the negative x-, y-, and z-directions:

$\bar{F}^e_{-50,x} = [-50, 0, 0]^T$, $\bar{F}^e_{-50,y} = [0, -50, 0]^T$, and

$\bar{F}^e_{-50,z} = [0, 0, -50]^T$.

Let $\delta_{-50,x}$, $\delta_{-50,y}$, and $\delta_{-50,z}$ be the deformation displacements at the node in the x-, y-, and z-directions, respectively. The fitting factors are set to 1 and 100 for the characteristic boundary parameters, respectively:

$a_1 = [a_A \ a_{I_y} \ a_{I_z} \ a_J]^T = [1 \ 1 \ 1 \ 1]^T$,

$a_2 = [100 \ 1 \ 1 \ 1]^T$, $a_3 = [1 \ 100 \ 1 \ 1]^T$, $a_4 = [1 \ 1 \ 100 \ 1]^T$,

and $a_5 = [1 \ 1 \ 1 \ 100]^T$.

The significance of each fitting factor to the deformation response is determined by comparing the percentage changes in $\delta_{-50,x}$, $\delta_{-50,y}$, and $\delta_{-50,z}$. The fitting sequence for the fitting factors is determined based on the characteristics of the significance of the deformation response. Table III summarizes the significance analysis of the deformation response of the stiffness model of the H–P robot. When a_A is increased 100-fold, the deformation displacements in the x-, y-, and z-directions become 12.94%, 103.27%, and 103.04% of the respective original values. Evidently, a_A has a significant and approximately inversely proportional impact on the x-direction. Similarly, a_{Iy} has a highly significant and approximately inversely proportional impact on the y-direction and a relatively weakly significant impact on the x- and z-directions. a_{Iz} has a relatively significant and approximately inversely proportional impact on the z-direction and a relatively weakly significant impact on the x- and y-directions. a_J has no significant impact on the x-, y-, or z-directions. By combining these findings, the following fitting sequence should be adopted: a_{Iy}, a_{Iz},a_A ,and a_J.

TABLE III
SIGNIFICANCE ANALYSIS OF THE DEFORMATION RESPONSE OF THE STIFFNESS MODEL OF THE H–P ROBOT

	a	Case	$\delta_{-50,x}$ (μm)	$\delta_{-50,y}$ (μm)	$\delta_{-50,z}$ (μm)	Significance analysis on the x-direction	Significance analysis on the y-direction	Significance analysis on the z-direction
$a_A = a_{Iy} = a_{Iz} = a_J = 1$	[1, 1, 1, 1]	1	-0.48	-9.00	-4472.00	/	/	/
Only $a_A = 100$	[100, 1, 1, 1]	2	-0.06	-9.29	-4608.00	/	/	/
Only $a_{Iy} = 100$	[1, 100, 1, 1]	3	-0.42	-0.15	-5513.00	/	/	/
Only $a_{Iz} = 100$	[1, 1, 100, 1]	4	-0.42	-9.92	-155.00	/	/	/
Only $a_J = 100$	[1, 1, 1, 100]	5	-0.48	-8.97	-4358.00	/	/	/
a_A	% of case 2/1	2/1	12.94	103.27	103.04	Highly significant	No significant	No significant
a_{Iy}	% of case 3/1	3/1	87.43	1.64	123.28	Significant	Highly significant	Significant
a_{Iz}	% of case 4/1	4/1	87.94	110.31	3.47	Significant	Significant	Relatively significant
a_J	% of case 5/1	5/1	99.85	99.68	97.45	No significant	No significant	No significant

IV. CASE STUDIES AND VALIDATION

A. SINGLE-POSE S-FSD MODEL AND ITS VALIDATION

Relatively reliable and accurate results can be obtained for a mechanism by FE simulation (i.e., establishing a non-FSD model). These results can be used to examine the correctness of theoretical calculation methods.[26] In this study, the 3D model of the H–P robot was imported into the ANSYS Workbench FE analysis software. Corresponding boundary conditions were then set. The H-P robot was fabricated with aluminum alloy. The joint bearings of the robot were made with bearing steel. The base of the robot was fixed onto the ground. A unidirectional external load was independently applied to the end of the robot in succession along each of the *x*-, *y*-, and z-directions. Tetrahedrons and hexahedrons were combined. The H–P robot was divided into 1,261,386 cells using the automatic mesh generation technique. "Bonded" contact conditions were applied to the robot mechanism.[27]

First, the fitting factors for the S-FSD model of the H–P robot were determined. Based on its structural composition, the H–P robot was divided into 36 cells. The pose of the H–P robot at point P_1 was selected. A unidirectional load of –50 N was applied to node F_8 at the end of the robot in succession along each of the negative *x*-, *y*-, and z-directions, i.e.,

$\bar{F}^{e}_{-50,x}=\left[-50,0,0\right]^{T}$, $\bar{F}^{e}_{-50,y}=\left[0,-50,0\right]^{T}$, and

$\bar{F}^{e}_{-50,z}=\left[0,0,-50\right]^{T}$.

Let $\delta_{-50,x}$, $\delta_{-50,y}$, and $\delta_{-50,z}$ be the deformation displacements at node F_8 in the *x*-, *y*-, and z-directions, respectively. The following results were obtained from FE simulation: $\delta_{-50,x}$=-2622μm, $\delta_{-50,y}$=-424.40μm, and $\delta_{-50,z}$ =-57.25μm, as shown in Table IV. Based on the results produced by the non-FSD model, a_{Iy}, a_{Iz},a_A , and a_J were fitted, in this sequence, using the Monte Carlo method. The following fitted values were obtained:a_{Iy}=0.0273,a_{Iz}=2.12,a_A=0.00645 ,and a_J=1.

Second, the results produced by the S-FSD model were verified against those produced by the non-FSD model. Unidirectional loads of –100N, –300N, and –500N were applied to the target node in succession along each of the negative *x*-, *y*-, and *z*-directions, i.e.,

$\bar{F}^{e}_{-100,x}=\left[-100,0,0\right]^{T}$, $\bar{F}^{e}_{-100,y}=\left[0,-100,0\right]^{T}$,

$\bar{F}^{e}_{-100,z}=\left[0,0,-100\right]^{T}$, $\bar{F}^{e}_{-300,x}=\left[-300,0,0\right]^{T}$,

$\bar{F}^{e}_{-300,y}=\left[0,-300,0\right]^{T}$, $\bar{F}^{e}_{-300,z}=\left[0,0,-300\right]^{T}$,

$\bar{F}^{e}_{-500,x}=\left[-500,0,0\right]^{T}$, $\bar{F}^{e}_{-500,y}=\left[0,-500,0\right]^{T}$, and

$\bar{F}^{e}_{-500,z}=\left[0,0,-500\right]^{T}$.

Table IV summarizes the results produced by the S-FSD and non-FSD models. Compared to the non-FSD model, which has 1,261,386 computational cells, the single-pose S-FSD model of the H–P robot has 99.9971% fewer computational cells—only 36 computational cells. In addition, compared to the non-FSD model, the S-FSD model requires at least 99.32% less computational time. The maximum difference between the deformation of the mechanism calculated by the S-FSD and that calculated by the non-FSD model is only 0.61%. The results produced by the S-FSD model are highly consistent with those produced by the non-FSD model. This validates the correctness of the S-FSD model.

TABLE IV
RESULTS FOR THE SINGLE-POSE S-FSD AND NON-FSD MODELS

Direction	Results	Case	δ_{-50} (μm)	δ_{-100} (μm)	δ_{-300} (μm)	δ_{-500} (μm)	t'_{-50} (s)	t'_{-100} (s)	t'_{-300} (s)	t'_{-500} (s)
x	Non-FSD model	1	-2622	-5240.9	-15698	-26134	724	864	1161	1309
	S-FSD model	2	-2624	-5248.2	-15745	-26241	3.33	3.27	3.27	3.34
y	Non-FSD model	3	-421.44	-842.81	-2526	-4211	561	564	563	564
	S-FSD model	4	-421.40	-842.93	-2529	-4215	3.38	3.55	3.34	3.3
z	Non-FSD model	5	-57.59	-115.18	-345.55	-575.91	494	491	496	497
	S-FSD model	6	-57.25	-114.8	-343.44	-572.4	3.27	3.34	3.36	3.33
x	% of case 2/1	2/1	100.08	100.14	100.30	100.41	0.46	0.38	0.28	0.26
y	% of case 4/3	4/3	99.99	100.01	100.12	100.09	0.60	0.63	0.59	0.59
z	% of case 6/5	6/5	99.43	99.67	99.39	99.39	0.66	0.68	0.68	0.67

B. MULTI-POSE S-FSD MODEL AND ITS VALIDATION

First, poses P'_{p1} and P'_{p3} of the H–P robot were selected for comprehensive fitting. Subsequently, poses P'_{p2} and P'_{p4} were selected to verify the results produced by the S-FSD model by comparison with those produced by the non-FSD model. Let K_{P1}, K_{P2}, K_{P3}, and K_{P4} be the stiffnesses of the H–P robot in the four extreme poses, respectively.

First, the fitting factors for the stiffness models of the H–P robot in the two poses were determined through simulation. The fitted values obtained in the previous section for the stiffness model of the H–P robot in pose P'_{p1} are as follows: a_{Iy}=0.0273,a_{Iz}=2.12,a_A=0.00645, and a_J=1. The following are the fitted values obtained for the stiffness model of the H–P robot in pose P'_{p3} using the same method: a_{Iy}=0.0300,a_{Iz}=1.95,a_A=0.00571,and a_J=1. By combining the fitted values for the fitting factors for poses P'_{p1} and P'_{p3}, the fitting factors were determined as follows: a_{Iy}=0.0285,a_{Iz}=2.025,a_A=0.00608 , and a_J=1.

Second, the S-FSD model was verified. Based on the non-FSD model, poses P'_{p2} and P'_{p4} of the H–P robot were selected. A unidirectional load of –50 N was applied to node F_8 at the end of the robot in succession along each of the *x*-, *y*-, and z-directions. The deformation displacements at the node at the end of the robot were calculated. Figures 5–7 show the deformation along the *x*-, *y*-, and z-directions, respectively, as obtained by the simulation.

This article has been accepted for publication in a future issue of this journal, but has not been fully edited. Content may change prior to final publication. Citation information: DOI 10.1109/ACCESS.2021.3063296, IEEE Access

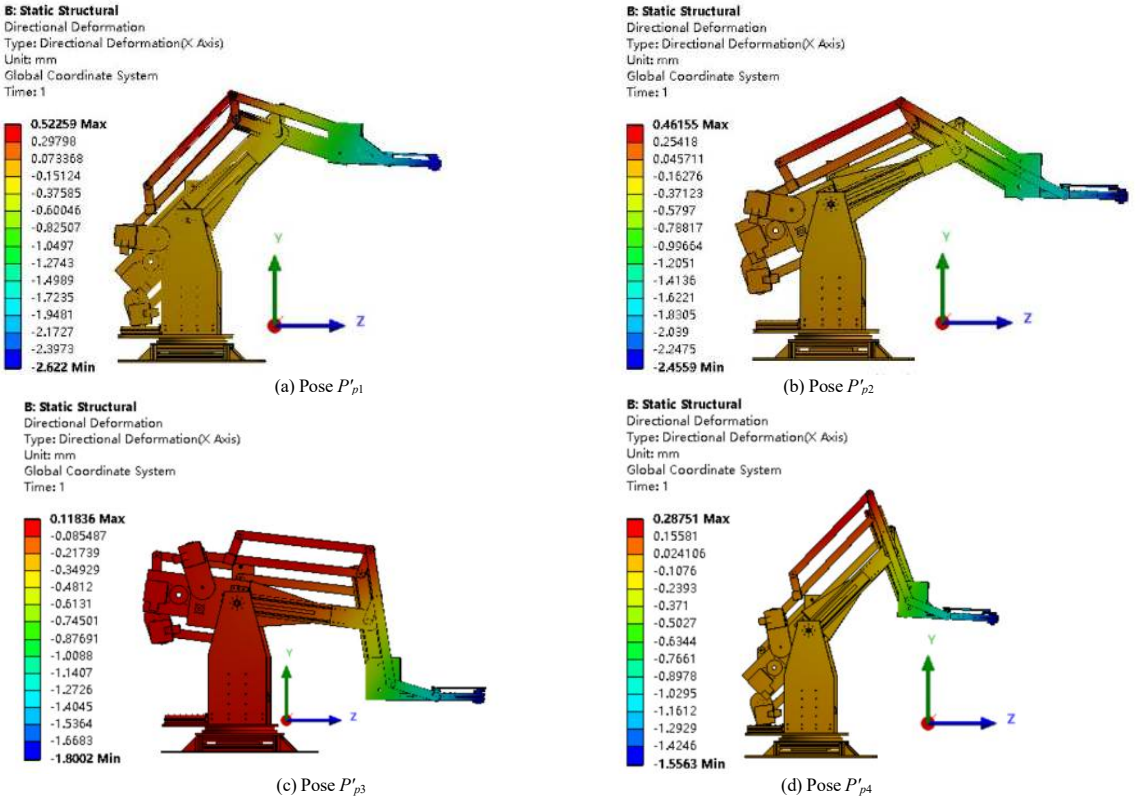

(a) Pose P'_{p1} (b) Pose P'_{p2}

(c) Pose P'_{p3} (d) Pose P'_{p4}

FIGURE 5. **Deformation along the x-direction.**

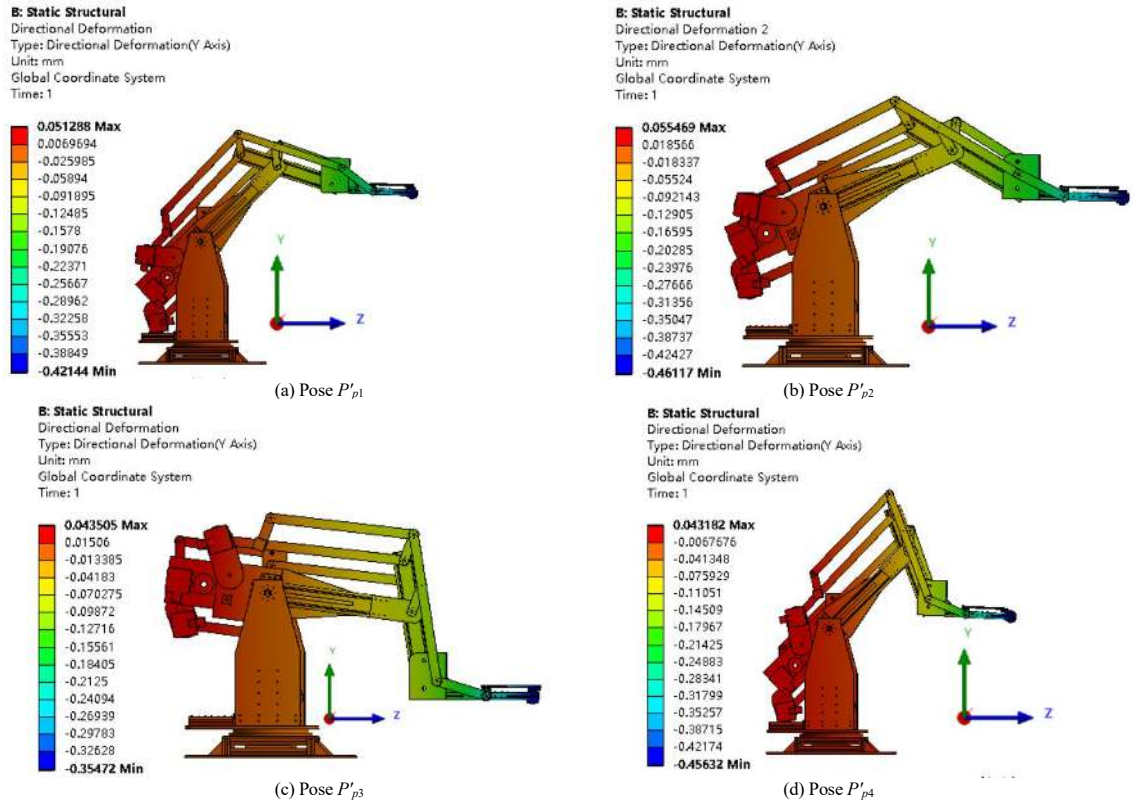

(a) Pose P'_{p1} (b) Pose P'_{p2}

(c) Pose P'_{p3} (d) Pose P'_{p4}

FIGURE 6. **Deformation along the y-direction.**

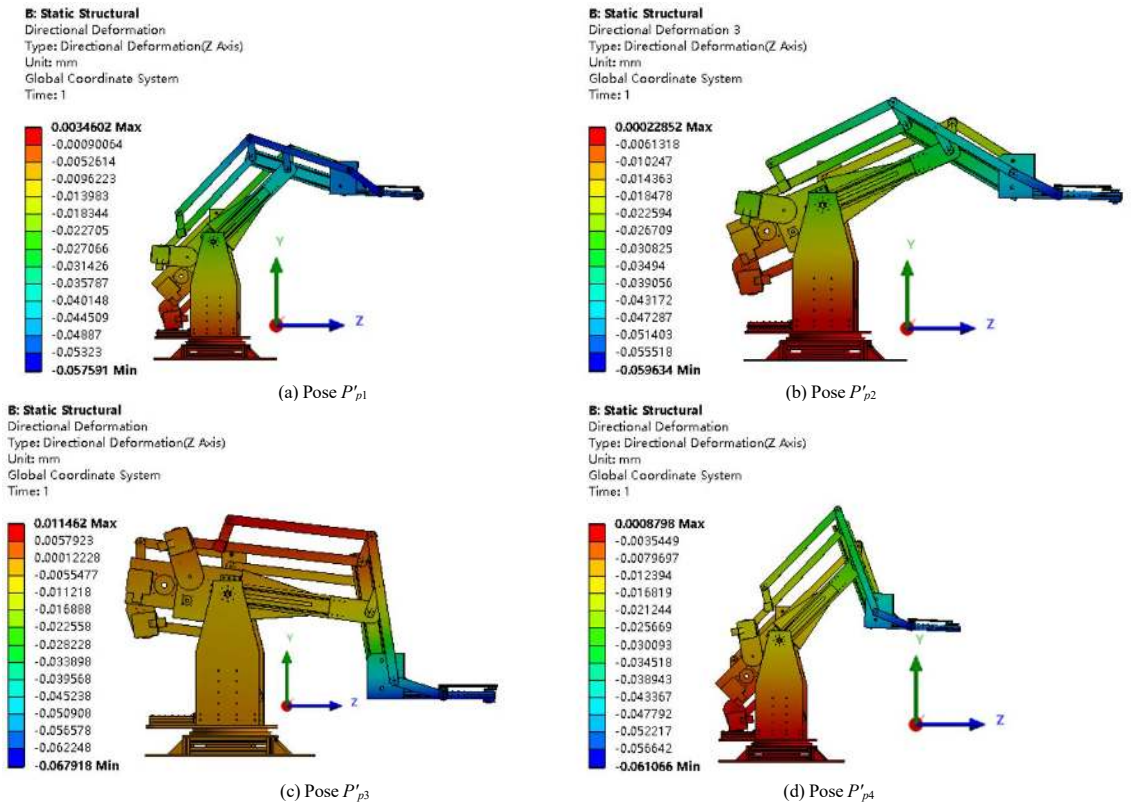

(a) Pose P'_{p1} (b) Pose P'_{p2}

(c) Pose P'_{p3} (d) Pose P'_{p4}

FIGURE 7. Deformation along the z-direction.

Table V summarizes the results produced by the S-FSD and non-FSD models. For the four poses of the H–P robot, the results produced by the non-FSD model are treated as reference values. For a unidirectional load applied along the *x*-direction, the values of $K_{P1,x}$, $K_{P2,x}$, $K_{P3,x}$, and $K_{P4,x}$ calculated by the S-FSD model are 95.19%, 104.80%, 105.40%, and 97.81% of those calculated by the non-FSD model, respectively. For a unidirectional load applied along the y-direction, the values of $K_{P1,y}$, $K_{P2,y}$, $K_{P3,y}$, and $K_{P4,y}$ calculated by the S-FSD model are 106.04 %, 113.75%, 83.06%, and 108.69% of those calculated by the non-FSD model, respectively. For a unidirectional load applied along the z-direction, the values of $K_{P1,z}$, $K_{P2,z}$, $K_{P3,z}$, and $K_{P4,z}$ calculated by the S-FSD model are 96.06 %, 95.58%, 102.59%, and 98.07% of those calculated by the non-FSD model, respectively. The maximum difference between the stiffnesses calculated by the S-FSD and non-FSD models is 16.94%. Evidently, the stiffnesses calculated by the S-FSD model are relatively close to those calculated by the non-FSD model. This validates the correctness of the multi-pose S-FSD model.

TABLE V
RESULTS FOR THE S-FSD AND NON-FSD MODELS

Direction	Results	Case	δ_{P1} (μm)	δ_{P2} (μm)	δ_{P3} (μm)	δ_{P4} (μm)	K_{P1} (N/μm)	K_{P2} (N/μm)	K_{P3} (N/μm)	K_{P4}(N/μm)
x	Non-FSD model	1	-57.59	-59.63	-67.92	-61.07	0.8682	0.8385	0.7362	0.8187
	S-FSD model	2	-60.50	-56.90	-64.44	-62.44	0.8264	0.8787	0.7759	0.8008
y	Non-FSD model	3	-421.44	-461.17	-354.72	-456.32	0.1186	0.1084	0.1410	0.1096
	S-FSD model	4	-397.44	-405.44	-427.07	-419.82	0.1258	0.1233	0.1171	0.1191
z	Non-FSD model	5	-2622.00	-2455.90	-1800.20	-1556.30	0.0191	0.0204	0.0278	0.0321
	S-FSD model	6	-2729.57	-2569.42	-1754.70	-1586.85	0.0183	0.0195	0.0285	0.0315
x	% of case 2/1	2/1	105.05	95.42	94.88	102.24	95.19	104.80	105.40	97.81
y	% of case 4/3	4/3	94.31	87.92	120.40	92.00	106.04	113.75	83.06	108.69
z	% of case 6/5	6/5	104.10	104.62	97.47	101.96	96.06	95.58	102.59	98.07

C. EXPERIMENT ON THE STRESS-INDUCED DEFORMATION OF THE H–P ROBOT IN MULTIPLE POSES

A prototype of the robot was fabricated with aluminum alloy. The joint bearings of the robot were made with bearing steel. The stiffness of the H–P robot in each pose was determined by applying a unidirectional load to the end of the H–P robot and measuring its deformation.

Figure 8 shows the experimental test platform. It is composed primarily of the H–P robot, a screw jack, a tension–compression dynamometer and its display, and a digital dial gauge. The jack was used to apply a unidirectional external load. One end of the jack was fixed onto a wall, while its other end was connected to the end of

This article has been accepted for publication in a future issue of this journal, but has not been fully edited. Content may change prior to final publication. Citation information: DOI 10.1109/ACCESS.2021.3063296, IEEE Access

the H–P robot via the dynamometer. The dynamometer was used to measure the magnitude of the applied load. In addition, the dial gauge was used to measure the deformation at the end of the robot along the direction in which the unidirectional load acted. Subsequently, the corresponding stiffness of the robot was calculated.

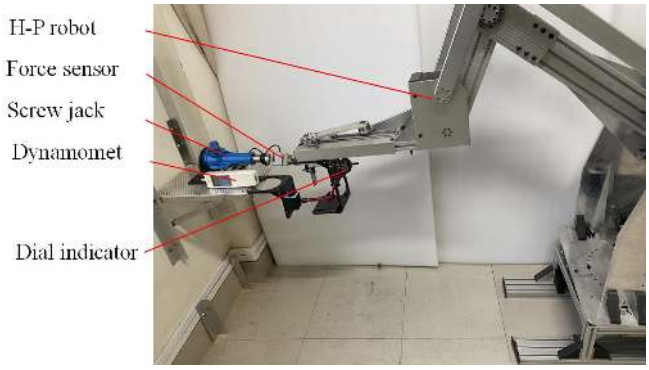

FIGURE 8. Experimental system to measure the end deformation of the H-P robot.

The H–P robot was set in succession in poses P'_{p1} , P'_{p2} , P'_{p3} , and P'_{p4}.Unidirectional loads of 0N, –10N, –20N, –30N, –40N, –50N, –60N, and –70N were applied to the target node in succession along each of the negative *x*-, *y*-, and *z*-directions. The experimental steps were as follows:

(1) Select the pose. The pose of the robot was adjusted to allow its end to reach the selected location.

(2) Select the direction. The base of the robot was fixed onto the ground. One end of the jack was fixed onto a wall. The pose of the robot was adjusted and locked.

(3) The dynamometer was mounted, and the dial gauge was initialized. Based on the first deformation (static deformation) caused by gravity, the second deformation (dynamic deformation) caused by external load is measured by experiment.Specifically, the jack and the dynamometer were mounted horizontally and slightly pressed against the robot. The reading of the dial gauge was zeroed.

(4) Select the unidirectional external load.The deformation at the end of the robot was measured. An external load was applied five times. For each direction and unidirectional load, five measurements were taken and were subsequently averaged and analyzed using error bars.

(5) Select the next unidirectional load(–10N to –70N) of the robot and repeat Step 4 .

(6) Select the next direction(*x*-, *y*-, and *z*-directions) of the robot and repeat Steps 2–5 .

(7) Select the next pose(P'_{p1} to P'_{p4}) of the robot and repeat Steps 1–6.

Figures 9 show the relationship between the external load and the deformation at the end of the robot along each direction at each location. As the external load increased, there was a gradual increase in the deformation of the H–P robot along each of the *x*-, *y*-, and *z*-directions. However, overall, the deformation along the *z*-direction was the least significant, the deformation along the x-direction was the most significant, and the deformation along the *y*-direction was between that along the *x*-direction and that along the *z*-direction. The stiffness of the robot was calculated based on the experimental data. For each direction,the seven values of the stiffness of the robot under the seven applications of the external load were averaged.Table VI summarizes the measured stiffnesses of the robot in the four poses (K_{P1}, K_{P2}, K_{P3}, and K_{P4}) along the three directions.

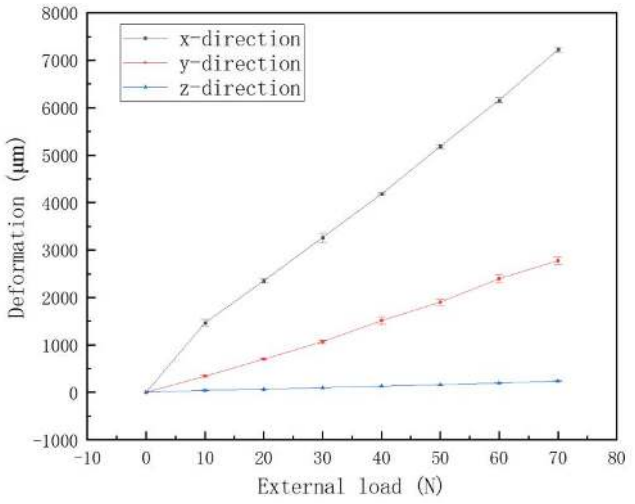

(a) Pose P'_{p1}

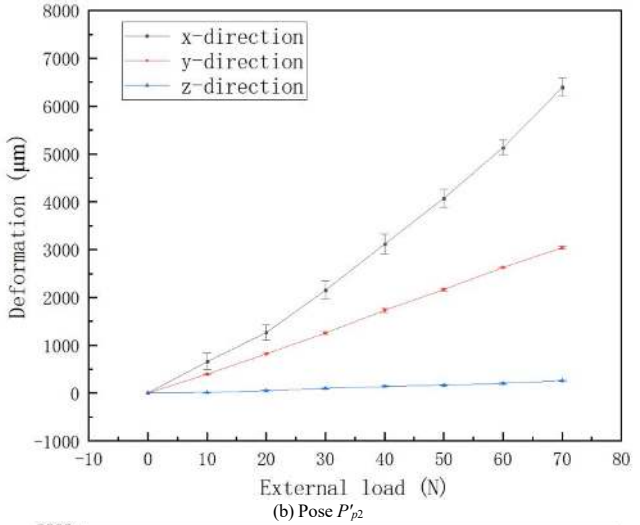

(b) Pose P'_{p2}

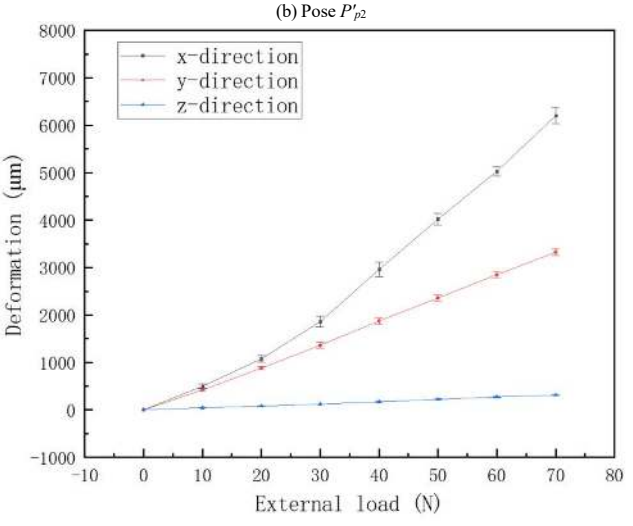

(c) Pose P'_{p3}

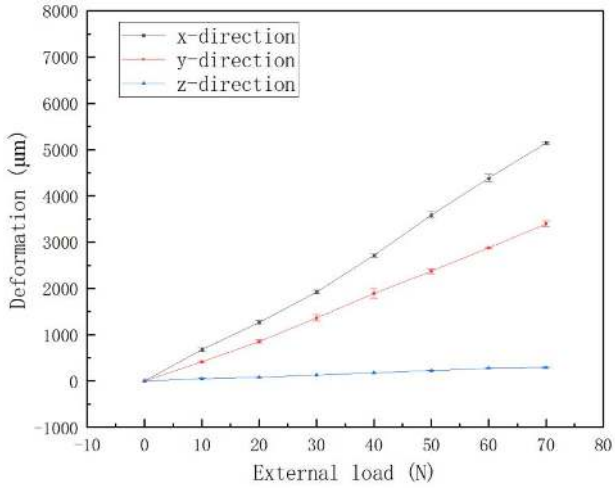

(d) Pose P'_{p4}

FIGURE 9. Relationship between the external load and the deformation at the end of the robot.

D. MULTI-POSE M-FSD MODEL AND ITS VALIDATION

Poses P'_{p1} and P'_{p3} of the H–P robot were selected for comprehensive experimental fitting. Subsequently, poses P'_{p2} and P'_{p4} were selected to verify the results produced by the M-FSD model by comparison with the experimental results.

The fitted values of the fitting factors obtained for the beam elements of the robot in pose P'_{p1} are as follows: a_{Iy}=0.006341,a_{Iz}=0.921375,a_A=0.004134 ,and a_J=1. The fitted values of the fitting factors for the beam elements of the robot in pose P'_{p3} are as follows: a_{Iy}=0.003374, a_{Iz}=1.007063, a_A=0.00168 , and a_J=1. By combining the fitted values of the fitting factors for poses P'_{p1} and P'_{p3}, the fitting factors for the beam elements of the robot were determined as follows:a_{Iy}=0.004857,a_{Iz}=0.964219,a_A=0.002997 ,and a_J=1. The fitting factors for the link elements of the robot are as follows: a_{Iy}=100,a_{Iz}=2.025,a_A=0.00608 ,and a_J=100.

The M-FSD model was verified. Poses P'_{p2} and P'_{p4} of the H–P robot were selected for verification. Table VI summarizes the results produced by the M-FSD model and the experimental results. For the four poses of the H–P robot, the experimental results are treated as reference values. For a unidirectional load applied along the *x*-direction, the values of $K_{P1,x}$, $K_{P2,x}$,$K_{P3,x}$,and $K_{P4,x}$ calculated by the M-FSD model are 91.59%, 86.82%, 110.57%, and 115.34% of their experimental values, respectively. For a unidirectional load applied along the y-direction, the values of $K_{P1,y}$, $K_{P2,y}$,$K_{P3,y}$,and $K_{P4,y}$ calculated by the M-FSD model are 99.19%, 111.79%, 115.85%, and 95.48% of their experimental values, respectively. For a unidirectional load applied along the z-direction, the values of $K_{P1,z}$, $K_{P2,z}$,$K_{P3,z}$,and $K_{P4,z}$ calculated by the M-FSD model are 105.08%, 78.33%, 86.49%, and 123.66% of their experimental values, respectively. The maximum and second maximum differences in stiffness are 23.66% and 22.67%, respectively. In all the other cases, the difference in stiffness is within 15.85%. Manifestly, the results produced by the M-FSD model of the H–P robot are relatively close to the experimental results. This validates the correctness of the multi-pose M-FSD model.

TABLE VI
RESULTS FROM THE M-FSD MODEL AND THE EXPERIMENTAL RESULTS

	Results	Case	K_{P1} (N/μm)	K_{P2} (N/μm)	K_{P3} (N/μm)	K_{P4} (N/μm)
x	Experiment	1	0.29181	0.33622	0.23271	0.22576
	M-FSD model	2	0.26727	0.29190	0.25730	0.26038
y	Experiment	3	0.02698	0.02365	0.02191	0.02187
	M-FSD model	4	0.02676	0.02644	0.02538	0.02542
z	Experiment	5	0.00902	0.01324	0.01485	0.01457
	M-FSD model	6	0.00948	0.01037	0.01284	0.01802
x	% of case 2/1	2/1	91.59	86.82	110.57	115.34
y	% of case 4/3	4/3	99.19	111.79	115.85	95.48
z	% of case 6/5	6/5	105.08	78.33	86.49	123.66

V. COMPARATIVE ANALYSIS AND DISCUSSION OF THE STIFFNESS OF THE H–P ROBOT

A. EVOLUTIONARY PROCESS FOR CONFIGURING THE H–P ROBOT MECHANISMS

To facilitate a comparative analysis of the effects of different branched chains on the stiffness of the H–P robot, six mechanisms (A, B, C, D, E, and F) were derived from an evolutionary process for configuring the H–P robot prototype, as shown in Figure 10. Each mechanism has four DOFs, achieved through a combination of axes 1, 2, 3, and 4, which correspond to actuators M_1, M_2, M_3, and M_4, respectively. The evolution of the configuration of the H–P robot involves two processes:

(1) Movement of the actuators: The drive motors that are originally on the right side of the host mechanism gradually move to the left side of the robot mechanism to compensate for gravity.

(2) Addition of parasitic branched chains: Adding parasitic branched chains gradually increases the structural stiffness of the mechanism to varying degrees.[25]

The fitting factors of the multi-pose M-FSD model of mechanism F were used for all six configurations. A total of 50,000 poses of the H–P robot within its working range were generated using the Monte Carlo method. The SD was analyzed based on the *x*-, *y*-, and *z*-directions.

Mechanism A is a serial mechanism with no parasitic branched chains and can serve as a host mechanism. Mechanism B is formed by adding a balancing parasitic branched chain (branched chain B) to mechanism A. Mechanism C is formed by adding a branched chain (branched chain C) that can drive axis 3 to mechanism B. Mechanism D is formed by adding a branched chain (branched chain D) that can drive axis 2 to mechanism C. Mechanism E is formed by adding branched chains (branched chains E and G) that can drive axis 1 to mechanism D. Mechanism F is formed by adding a branched chain (branched chain F) that can drive axis 4 to mechanism E.

This article has been accepted for publication in a future issue of this journal, but has not been fully edited. Content may change prior to final publication. Citation information: DOI 10.1109/ACCESS.2021.3063296, IEEE Access

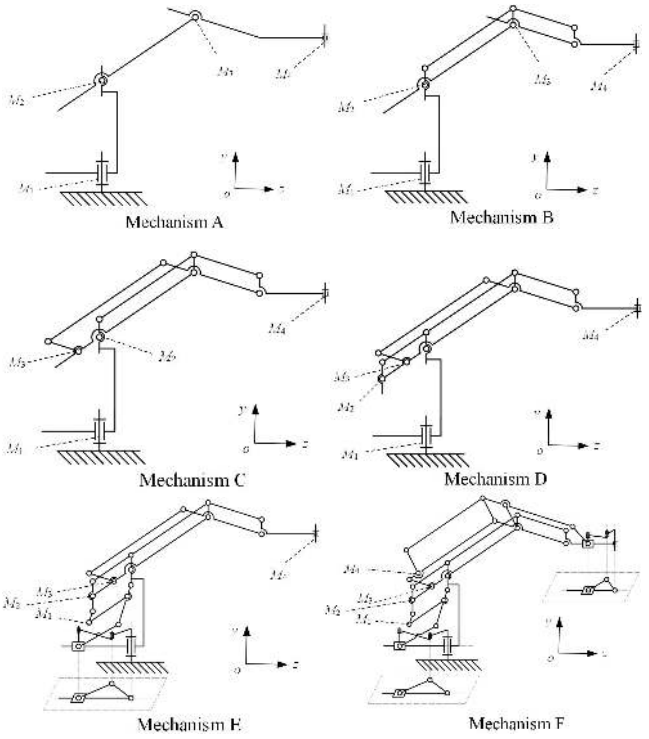

FIGURE 10. **The six mechanisms of the H–P robot.**

B. COMPARISON OF THE SDS IN THE X-DIRECTION

The characteristic parameters of the SDs of the six mechanisms in the x-direction include the minimum stiffness $K_{min,x}$, the maximum stiffness $K_{max,x}$, the difference in stiffness ΔK_x, and the average stiffness $\bar{K}_x$ (Table VII). A comparison of mechanisms B–D with mechanism A shows that the four characteristic parameters increase slightly as the number of branched chains increases. The most significant increase in the four characteristic parameters is for mechanism F. $K_{min,x}$, $K_{max,x}$, ΔK_x, and K_x of mechanism F are 104.44%, 104.05%, 103.61%, and 104.1% of those of mechanism A, respectively.

TABLE VII
COMPARISON OF THE SDS IN THE X-DIRECTION

	Case	$K_{min,x}$ (N/μm)	$K_{max,x}$ (N/μm)	ΔK_x (N/μm)	$\bar{K}_x$ (N/μm)
Mechanism A	1	0.0090	0.0173	0.0083	0.0122
Mechanism B	2	0.0091	0.0178	0.0086	0.0124
Mechanism C	3	0.0094	0.0182	0.0088	0.0128
Mechanism D	4	0.0094	0.0182	0.0088	0.0128
Mechanism E	5	0.0090	0.0172	0.0081	0.0120
Mechanism F	6	0.0094	0.0188	0.0086	0.0127
% of case 2/1	2/1	101.11	102.89	103.61	101.64
% of case 3/1	3/1	104.44	105.20	106.02	104.92
% of case 4/1	4/1	104.44	105.20	106.02	104.92
% of case 5/1	5/1	100.00	99.42	97.59	98.36
% of case 6/1	6/1	104.44	104.05	103.61	104.10

Figures 11–16 are 3D and two-dimensional (2D) SD diagrams of the six mechanisms. There are considerable similarities between their SDs. The high-stiffness region is concentrated near the nearest pose point P_4. The low-stiffness region is concentrated near the highest pose point P_1 and the furthest pose point P_2. The medium-stiffness region is relatively large. Adding parasitic branched chains only slightly improves the SD of the H–P robot in the x-direction.

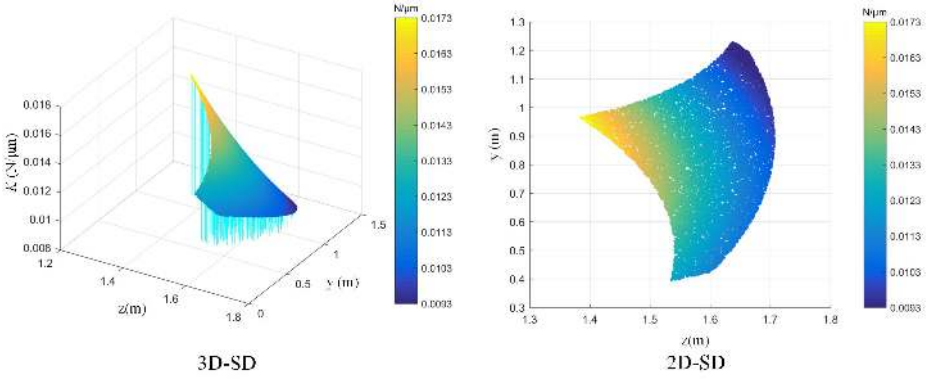

FIGURE 11. **SDs of the mechanism A robot in the x-direction.**

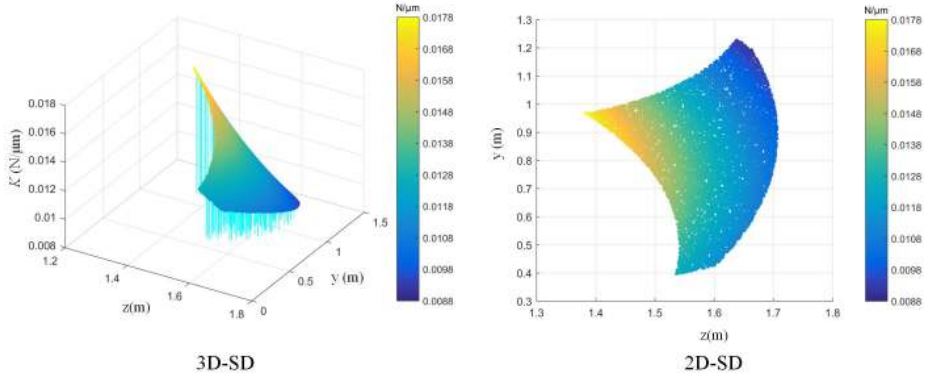

FIGURE 12. **SDs of the mechanism B robot in the x-direction.**

This article has been accepted for publication in a future issue of this journal, but has not been fully edited. Content may change prior to final publication. Citation information: DOI 10.1109/ACCESS.2021.3063296, IEEE Access

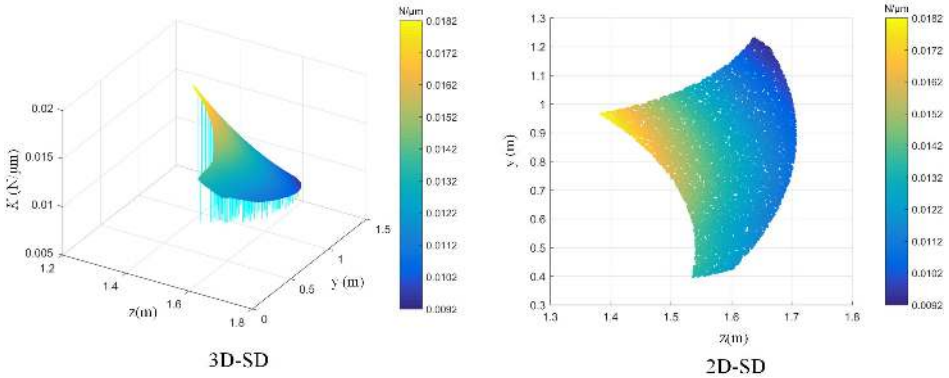

FIGURE 13. **SDs of the mechanism C robot in the x-direction.**

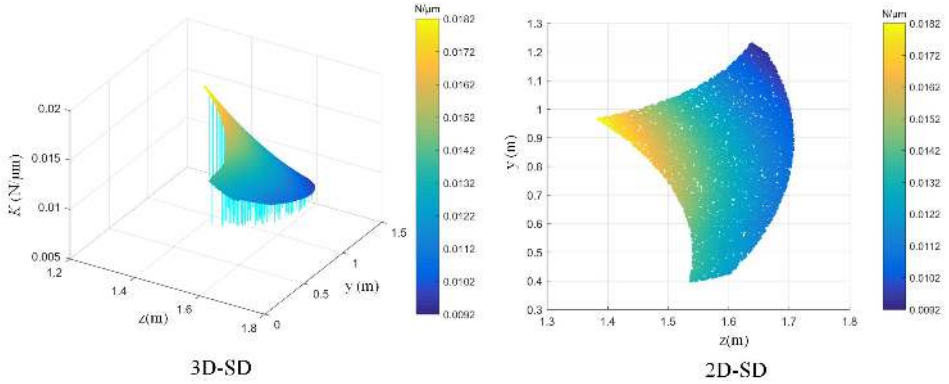

FIGURE 14. **SDs of the mechanism D robot in the x-direction.**

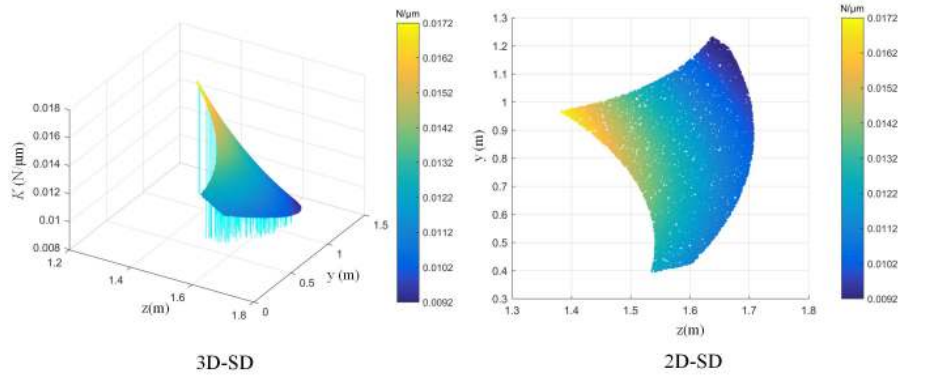

FIGURE 15. **SDs of the mechanism E robot in the x-direction.**

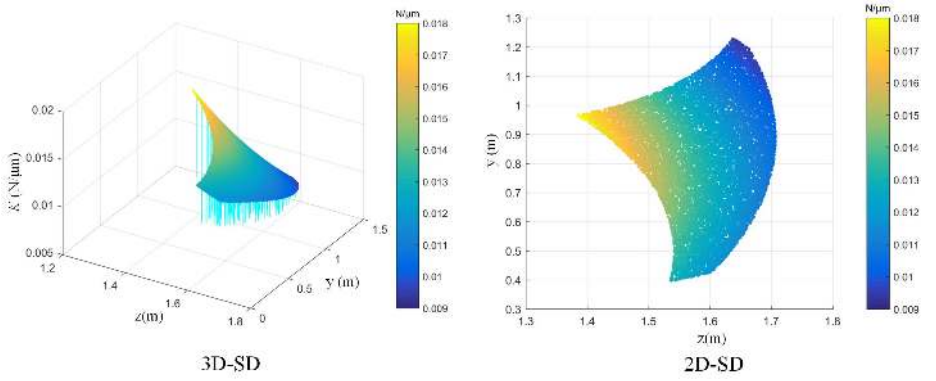

FIGURE 16. **SDs of the mechanism F robot in the x-direction.**

C. COMPARISON OF THE SDS IN THE *Y*-DIRECTION

The characteristic parameters of the SD of the six mechanisms in the y-direction include the minimum stiffness $K_{min,y}$, the maximum stiffness $K_{max,y}$, the difference in stiffness ΔK_y, and the average stiffness $\overline{K}_y$ (Table VIII). A comparison of mechanisms B–F with mechanism A shows the following. Of the four characteristic parameters, $K_{max,y}$

This article has been accepted for publication in a future issue of this journal, but has not been fully edited. Content may change prior to final publication. Citation information: DOI 10.1109/ACCESS.2021.3063296, IEEE Access

and ΔK_y decrease as the number of branched chains increases. The most significant decreases in $K_{max,y}$ and ΔK_y are for mechanisms C and D. Specifically, $K_{max,y}$ and ΔK_y for mechanisms C and D are 5.82% and 1.85% of those of mechanism A, respectively. In contrast, $K_{min,y}$ increases significantly as the number of branched chains increases. The most significant increase in $K_{min,y}$ is for mechanism F. Specifically, $K_{min,y}$ and $\bar{K}_y$ of mechanism F are 5456.52% and 1427.78% of those of mechanism A, respectively.

TABLE VIII
COMPARISON OF THE SDS IN THE Y-DIRECTION

	Case	$K_{min,y}$ (N/μm)	$K_{max,y}$ (N/μm)	ΔK_y (N/μm)	$\bar{K}_y$ (N/μm)
Mechanism A	1	0.00046	0.0275	0.0271	0.0018
Mechanism B	2	0.00054	0.0015	0.0010	0.0010
Mechanism C	3	0.00110	0.0016	0.0005	0.0013
Mechanism D	4	0.00110	0.0016	0.0005	0.0013
Mechanism E	5	0.00130	0.0038	0.0025	0.0018
Mechanism F	6	0.02510	0.0265	0.0150	0.0258
% of case 2/1	2/1	117.39	5.45	3.69	55.56
% of case 3/1	3/1	239.13	5.82	1.85	72.22
% of case 4/1	4/1	239.13	5.82	1.85	72.22
% of case 5/1	5/1	282.61	13.82	9.23	100.00
% of case 6/1	6/1	5456.52	96.73	55.35	1427.78

Figures 17–22 are the 3D and 2D SD diagrams of the six mechanisms. The SD of mechanism A is not ideal. Specifically, the SD of mechanism A varies significantly. The high-stiffness region of mechanism A is small and concentrated near the nearest pose point P_4, whereas its low-stiffness region is large. Both the low- and high-stiffness regions of mechanism B are relatively small and concentrated near the lowest pose point P_3 and the furthest pose point P_4, respectively. The medium-stiffness region of mechanism B is relatively large. The SDs of mechanisms C and D vary insignificantly. For mechanisms C and D, the high-stiffness region is concentrated near the highest pose point P_1, and the medium-stiffness region is relatively large. The high-stiffness region of mechanism E is concentrated near the lowest pose point P_3, and its low-stiffness region is large. Mechanism F has the most ideal SD and the highest average stiffness. Mechanism F has a relatively large high-stiffness region, which is distributed in a banded pattern between the furthest pose point P_2 and the highest pose point P_1 and extends to near the lowest pose point P_3. In addition, mechanism F has a relatively large medium-stiffness region. This suggests that adding parasitic branched chains can significantly improve the SD of the H–P robot in the y-direction and that branched chain F, in particular, produces the most significant improvement.

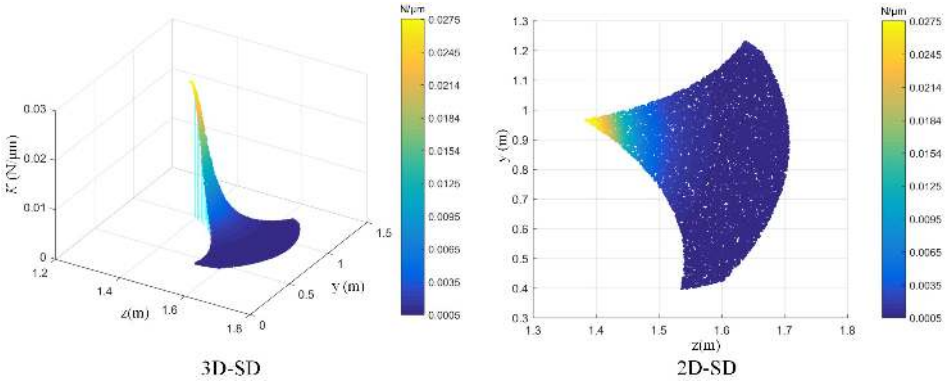

FIGURE 17. **SDs of the mechanism A robot in the *y*-direction.**

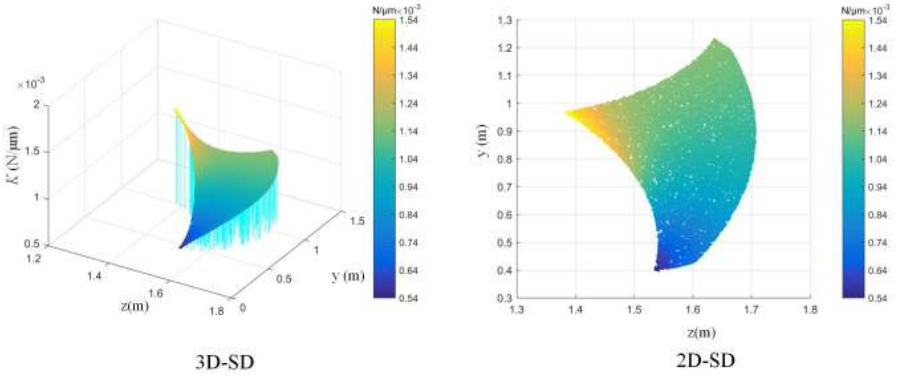

FIGURE 18. **SDs of the mechanism B robot in the *y*-direction.**

This article has been accepted for publication in a future issue of this journal, but has not been fully edited. Content may change prior to final publication. Citation information: DOI 10.1109/ACCESS.2021.3063296, IEEE Access

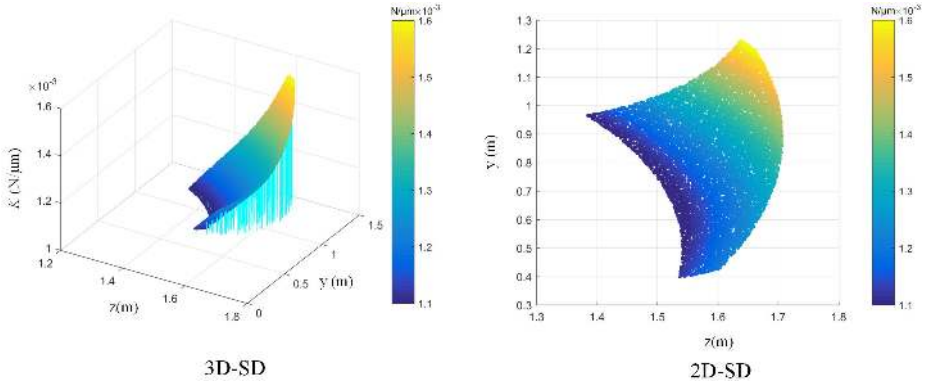

FIGURE 19. **SDs of the mechanism C robot in the *y*-direction.**

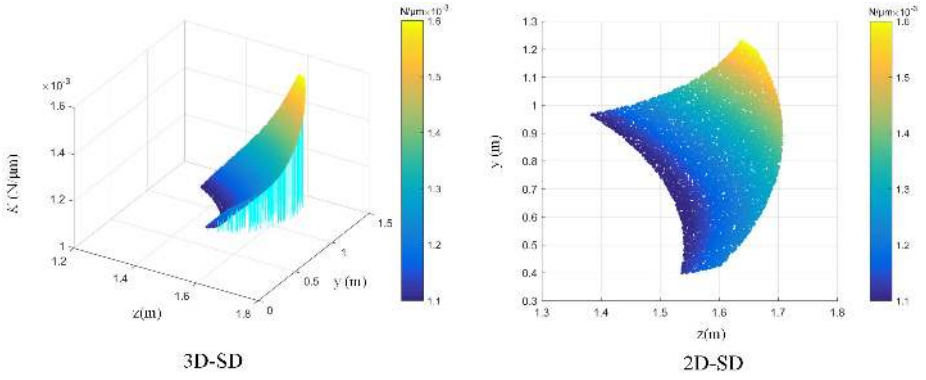

FIGURE 20. **SDs of the mechanism D robot in the *y*-direction.**

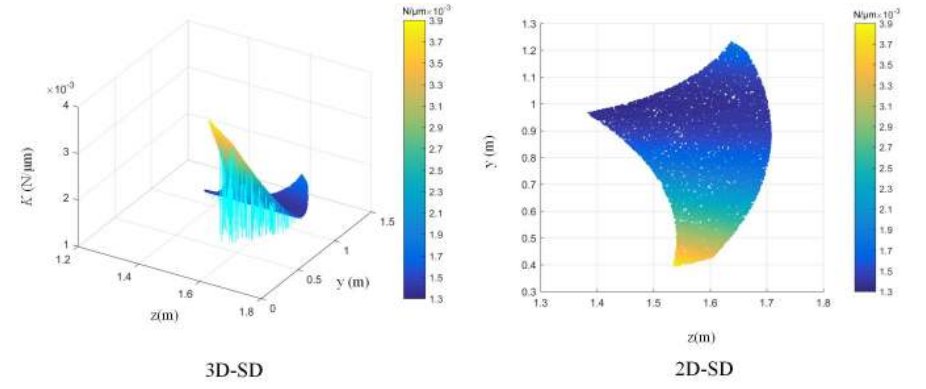

FIGURE 21. **SDs of the mechanism E robot in the *y*-direction.**

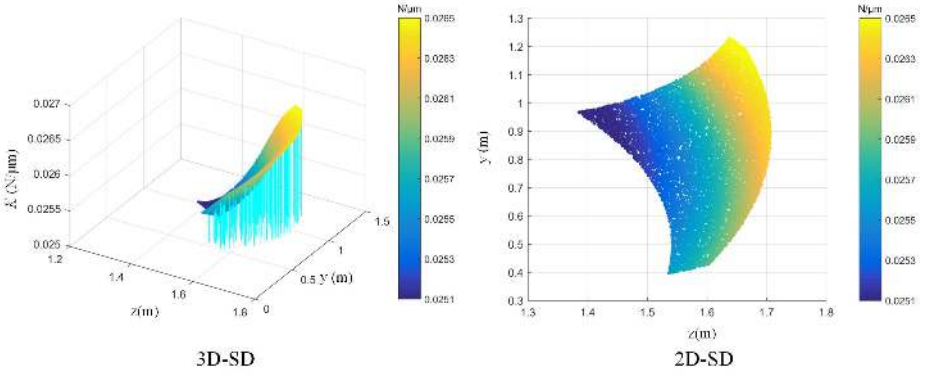

FIGURE 22. **SDs of the mechanism F robot in the *y*-direction.**

D. COMPARISON OF THE SDS IN THE *Z*-DIRECTION

The characteristic parameters of the SD of the six mechanisms in the z-direction include the minimum stiffness $K_{min,z}$, the maximum stiffness $K_{max,z}$, the difference in stiffness ΔK_z, and the average stiffness $\overline{K}_z$ (Table IX). A comparison of mechanisms B–F with mechanism A shows the following.

Of the four characteristic parameters, $K_{min,z}$ and $\bar{K}_z$ increase significantly as the number of branched chains increases. The most significant increase in $K_{min,z}$ and $\bar{K}_z$ is for mechanism F. Specifically, $K_{min,z}$ and $\bar{K}_z$ of mechanism F are 1923.31% and 1101.62% of those of mechanism A, respectively. In contrast, ΔK_z decreases significantly as the number of branched chains increases. The most significant decreases in ΔK_z are for mechanisms C and D. Specifically, ΔK_z for mechanisms C and D is 1.39% of that of mechanism A. $K_{max,z}$ increases or decreases slightly as the number of branched chains increases.

TABLE IX
COMPARISON OF THE SDS IN THE *Z*-DIRECTION

	Case	$K_{min,z}$ (N/μm)	$K_{max,z}$ (N/μm)	ΔK_z (N/μm)	$\bar{K}_z$ (N/μm)
Mechanism A	1	0.0133	0.2648	0.2515	0.0247
Mechanism B	2	0.2354	0.2480	0.0126	0.2456
Mechanism C	3	0.2446	0.2482	0.0035	0.2463
Mechanism D	4	0.2446	0.2482	0.0035	0.2463
Mechanism E	5	0.2435	0.2856	0.0422	0.2556
Mechanism F	6	0.2558	0.2905	0.0347	0.2721
% of case 2/1	2/1	1769.92	93.66	5.01	994.33
% of case 3/1	3/1	1839.10	93.73	1.39	997.17
% of case 4/1	4/1	1839.10	93.73	1.39	997.17
% of case 5/1	5/1	1830.83	107.85	16.78	1034.82
% of case 6/1	6/1	1923.31	109.71	13.80	1101.62

Figures 23–28 are the 3D and 2D SD diagrams of the six mechanisms. The SD of mechanism A is again unideal. Specifically, mechanism A is deficient as its SD pattern varies significantly. Its high-stiffness region is small and concentrated near the lowest pose point P_4, and it has a large low-stiffness region. The SD of mechanism B is relatively ideal. Mechanism B has a low-stiffness region that is small and concentrated near the lowest pose point P_4, a relatively large high-stiffness region, and a notably higher average stiffness than mechanism A. For mechanisms C, D, and E, the SD varies insignificantly, the low-stiffness region is small and concentrated near the lowest pose point P_3, the high-stiffness region is concentrated near the highest pose point P_1, and the medium-stiffness region is relatively large. The SD of mechanism F is the most ideal. Mechanism F has the highest average stiffness, a high-stiffness region that is relatively large and distributed in a banded pattern near the furthest pose point P_2 and the highest pose point P_1, and a relatively large medium-stiffness region. The stiffness of mechanism F decreases slightly near the highest pose point P_1. This suggests that adding parasitic branched chains can significantly improve the SD of the robot in the *z*-direction.

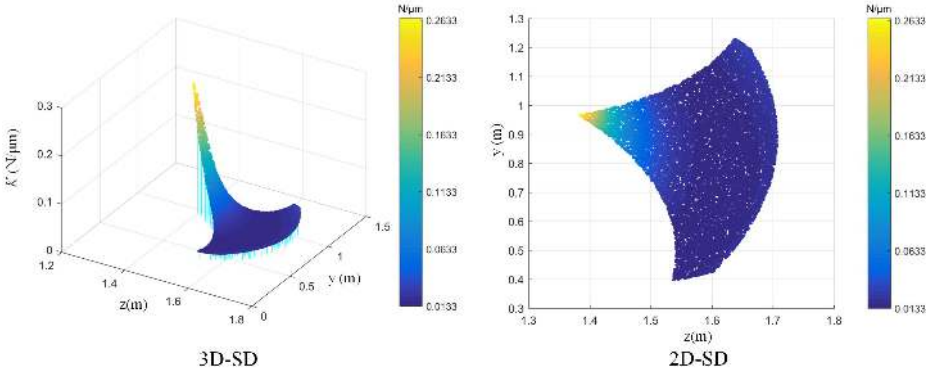

FIGURE 23. **SDs of the mechanism A robot in the *z*-direction.**

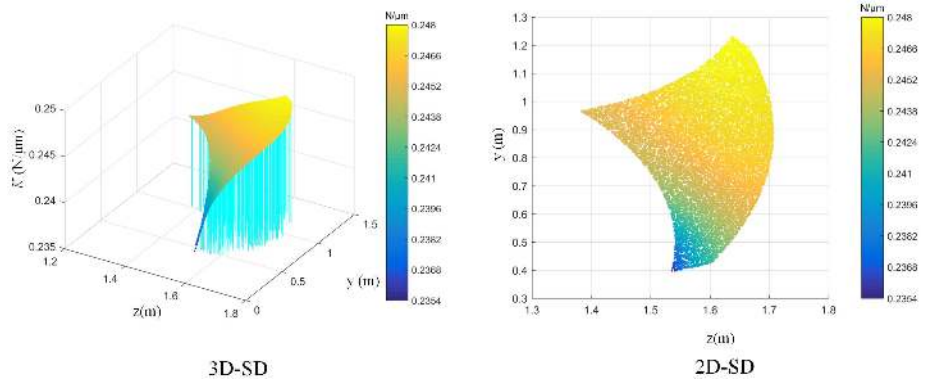

FIGURE 24. **SDs of the mechanism B robot in the *z*-direction.**

This article has been accepted for publication in a future issue of this journal, but has not been fully edited. Content may change prior to final publication. Citation information: DOI 10.1109/ACCESS.2021.3063296, IEEE Access

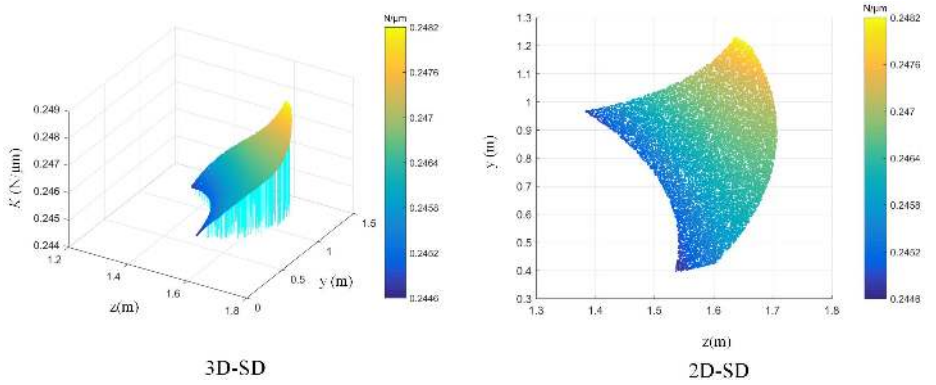

FIGURE 25. **SDs of the mechanism C robot in the *z*-direction.**

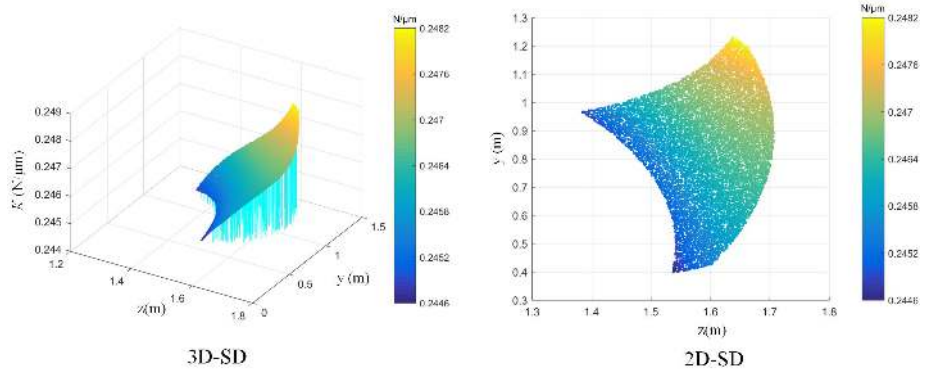

FIGURE 26. **SDs of the mechanism D robot in the *z*-direction.**

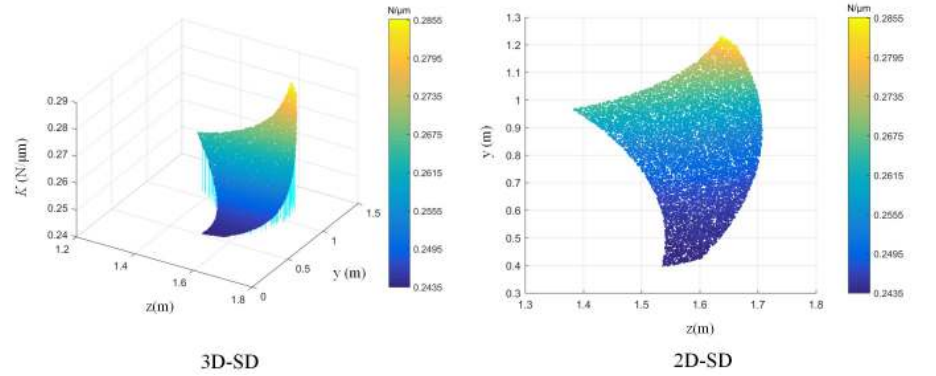

FIGURE 27. **SDs of the mechanism E robot in the *z*-direction.**

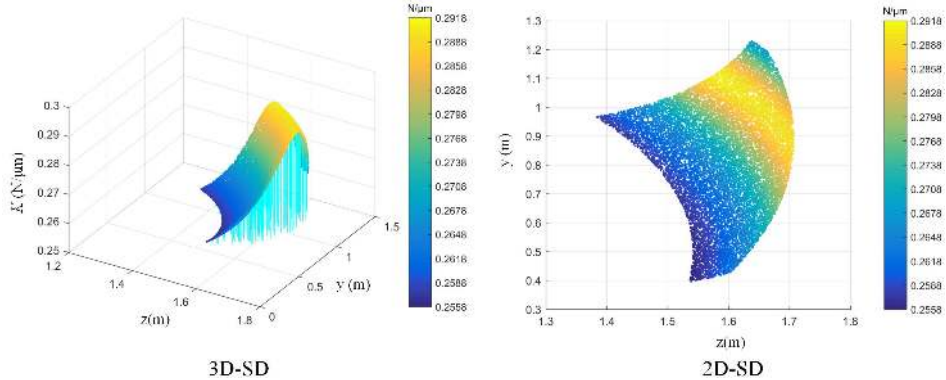

FIGURE 28. **SDs of the mechanism F robot in the *z*-direction.**

E. COMPARISON OF THE STIFFNESSES IN DIFFERENT DIRECTIONS

The SD in the x-direction varies relatively insignificantly between the six mechanism (Table X). Thus, the average stiffness in the x-direction $\bar{K}_x$ is selected as a reference for

comparison. $\bar{K}_y$ and $\bar{K}_z$ for mechanism A are 14.75% and 202.46% of its $\bar{K}_x$, respectively. Adding parasitic branched chains considerably increases $\bar{K}_z$, as evidenced for mechanisms B, C, D, and E. Specifically, $\bar{K}_z$ of mechanisms B, C, D, and E is 1980.65%, 1924.22%, 1924.22%, and 2130.00% of $\bar{K}_x$, respectively. $\bar{K}_y$ of mechanisms B, C, D, and E is close to that of mechanism A. $\bar{K}_y$ of each of mechanisms B, C, D, and E is 8.06%, 10.16%, 10.16%, and 15.00% of its $\bar{K}_x$, respectively. Adding parasitic branched chain F significantly increases both $\bar{K}_y$ and $\bar{K}_z$, as evidenced in mechanism F. $\bar{K}_y$ and $\bar{K}_z$ of mechanism F are 202.36% and 2142.52% of its $\bar{K}_x$, respectively. Clearly, adding parasitic branched chains can improve the average stiffnesses of the mechanism in the *y*- and *z*-directions to varying degrees.

TABLE X
COMPARISON OF THE STIFFNESSES IN DIFFERENT DIRECTIONS

	Case	Mechanism A	Mechanism B	Mechanism C	Mechanism D	Mechanism E	Mechanism F
K_x (N/μm)	1	0.0122	0.0124	0.0128	0.0128	0.012	0.0127
K_y (N/μm)	2	0.0018	0.001	0.0013	0.0013	0.0018	0.0257
K_z (N/μm)	3	0.0247	0.2456	0.2463	0.2463	0.2556	0.2721
% of case 2/1	2/1	14.75	8.06	10.16	10.16	15.00	202.36
% of case 3/1	3/1	202.46	1980.65	1924.22	1924.22	2130.00	2142.52

VI. CONCLUSIONS

Accurately calculating the stiffnesses at the end of a complex robot for all of its poses is relatively expensive in terms of time cost. This study presents an FE fitting method that uses an extremely small number of mesh cells in modeling. This method was used to establish FSD models for an H–P robot, which facilitated an efficient and accurate calculation and analysis of the SD of its different evolutionary mechanisms.

(1) The link and beam elements of an H–P robot are identified and classified as well as fitted in different ways.The S-FSD and M-FSD modeling methods proposed in this study can be used to facilitate a parallel calculation of the stiffnesses at the end of a complex robot in almost all the poses within its working range.

(2) Compared to the conventional non-FSD model, the S-FSD model requires at least 99.32% less computational time. The multi-pose M-FSD model established in this study contains significantly fewer computational cells and requires significantly less computational time while being able to produce results that agree relatively well with the experimental results.

(3) The locations and sizes of the low-, medium-, and high-stiffness regions of the six H–P mechanisms can be directly determined from the SD diagrams produced by the M-FSD model.Adding parasitic branched chains can improve the SD of the H–P robot. In particular, the most notable improvement was for mechanism F.

(4) This method can provide a foundation for the structural design and optimization of new robots.For example,a design of flexible joint robot manipulator or PAM(Pneumatic Artificial Muscle) actuated manipulator,DLCC (Dynamic Load Carrying Capacities) analysis of robot,and pose accuracy analysis of robot under different working loads.

REFERENCES

[1] V. T. Portman, "Stiffness evaluation of machines and robots: minimum collinear stiffness value approach," *J. Mechanisms Robotics.,* vol. 3, no. 1, Feb. 2011.

[2] H. Al-Dois, A. Jha, and R. Mishra, "Task-based design optimization of serial robot manipulators," *Eng. Optimiz.,* vol. 45, no. 6, pp. 647-658, Nov. 2013.

[3] H. Sun, Y. Zhang, B. Xie, and B. Zi, "Dynamic modeling and error analysis of a cable-linkage serial-parallel palletizing robot," *IEEE Access,* vol. 9, pp. 2188-2200, Dec. 2021.

[4] D. Erez, S. Arogeti, and D. Zarrouk, "A Novel Simple Two-Robot Precise Self-Localization Method," *IEEE Access,* vol. 7, pp. 154044-154055, Sep. 2019.

[5] P. Xiao, H. Ju, Q. Li, J. Meng, and F. Chen, "A new fixed axis-invariant based calibration approach to improve absolute positioning accuracy of manipulators," *IEEE Access,* vol. 8, pp. 134224-134232, July 2020.

[6] Y. Chen and F. Dong, "Robot machining: recent development and future research issues," *Int. J. Adv. Manuf. Tech.,* vol. 66, no. 9-12, pp. 1489-1497, July 2013.

[7] Y. Liu, D. Wang, S. Yang, J. Liu, and G. Hao, "Design and experimental study of a passive power-source-free stiffness-self-adjustable mechanism," *Front. Mech. Eng-Prc.,* pp. 1-14, Dec. 2020.

[8] A. L. Orekhov and N. Simaan, "Directional stiffness modulation of parallel robots with kinematic redundancy and variable stiffness joints," *J. Mech. Robot.,* vol. 11, no. 5, Oct. 2019.

[9] B. Chen, Z. Cui, and H. Jiang, "Producing negative active stiffness in redundantly actuated planar rotational parallel mechanisms," *Mech. Mach. Theory,* vol. 128, pp. 336-348, Oct. 2018.

[10] S. Jin, J. Kim, and T. Seo, "Optimization of a redundantly actuated 5R symmetrical parallel mechanism based on structural stiffness," *Robot,* vol. 33, no. 9, p. 1973, Nov 2015.

[11] K. Li, H. Jiang, and Z. Cui, "Design for solving negative stiffness problem of redundant planar rotational parallel mechanisms," *Int. J. Robot Autom.,* vol. 34, no. 1, 2019.

[12] M. Wang, P. Wang, Y. Song, X. Zhao, and T. Huang, "Stiffness analysis of a 4-DOF hybrid robot," *Chin. J. Mech. Eng-En.,* vol. 47, no. 15, pp. 9-16, 2011.

[13] J. Wu, J. Wang, L. Wang, T. Li, and Z. You, "Study on the stiffness of a 5-DOF hybrid machine tool with actuation redundancy," *Mech. Mach. Theory,* vol. 44, no. 2, pp. 289-305, Feb. 2009.

[14] S. Huang and J. M. Schimmels, "The eigenscrew decomposition of spatial stiffness matrices," *IEEE Trans. Robot. Auto.,* vol. 16, no. 2, pp. 146-156, Apr 2000.

[15] G. Wu, "Stiffness analysis and optimization of a co-axial spherical parallel manipulator," *Model. Ident. Control,* vol. 35, no. 1, pp. 21-30, 2014.

[16] K. Li, H. Jiang, S. Wang, and J. Yu, "A soft robotic fish with variable-stiffness decoupled mechanisms," *J. Bionic. Eng.,* vol. 15, no. 4, pp. 599-609, July 2018.

[17] B. He, S. Xu, and Z. Wang, "A novel stiffness model for a wall-climbing hexapod robot based on nonlinear variable stiffness," *Adv. Mech. Eng.,* vol. 10, no. 1, p. 1687814017752485, Jan 2018.

[18] Y. Yu, S. Wei, Q. Ji, and Z. Yang, "Design, Dynamics Analysis, and Real-Time Stiffness Control of a Variable Stiffness Joint," *Electronics,* vol. 9, no. 6, p. 973, June 2020.

[19] S.-k. Lu, D.-x. Hua, Y. Li, F.-y. Cui, and P.-y. Li, "Stiffness calculation method and stiffness characteristic analysis of bolted connectors," *Math. Probl. Eng.,* vol. 2019, Aug. 2019.
[20] X. Liu, C. Sun, J. R. Banerjee, H.-C. Dan, and L. Chang, "An exact dynamic stiffness method for multibody systems consisting of beams and rigid-bodies," *Mech. Syst. Signal Pr.,* vol. 150, p. 107264, March 2021.
[21] J. Zhang, Y. Zhao, and J. Dai, "Compliance modeling and analysis of a 3-RPS parallel kinematic machine module," *Chin. J. Mech. Eng-En.,* vol. 27, no. 4, pp. 703-713, Aug 2014.
[22] Q. Li, M. Wang, T. Huang, and D. G. Chetwynd, "Compliance analysis of a 3-DOF spindle head by considering gravitational effects," *Chin. J. Mech. Eng-En.,* vol. 28, no. 1, pp. 1-10, Dec. 2015.
[23] D. Sharma, N. Singh, H. Singh, and S. Rath, "Copro-prevalence and risk factor assessment of gastrointestinal parasitism in Indian domestic pigs," *Helminthologia,* vol. 57, no. 1, pp. 28-36, 2020.
[24] X. Cheng, *Human parasitology*. Shanghai: Fudan University Press, 2015.
[25] W. Wei, G. Cai, J. Gong, and C. Ban, "A host–parasite structural analysis of industrial robots," *Int. J. Adv. Robot Syst.,* vol. 17, no. 5, p. 1729881420954043, Oct. 2020.
[26] A. V. Nguyen, B. C. Bouzgarrou, K. Charlet, and A. Béakou, "Static and dynamic characterization of the 6-Dofs parallel robot 3CRS," *Mech. Mach. Theory,* vol. 93, pp. 65-82, Nov. 2015.
[27] L.Sun, L.Fang, and F.Liang, "Structure Design and Global Stiffness Prediction Method of a Novel Industrial Robot," *Robot,* vol. 40, no. 5, pp. 673-685, Sep.2018.

WEI WEI was born in 1984. He received the B.S. and M.S. degrees from Guangxi University, Nanning, China, in 2007 and 2010, respectively. He is currently pursuing the Ph.D. degree with South China University of Technology, China. His research interests include bionic robot design, and host–parasite mechanism, and spatial multi loop coupling mechanism.

GANWEI CAI was born in 1961. He received the Ph.D. degree in Huazhong University of science and technology, China, in 1998. He was a postdoctoral researcher in Central South University, China, in 1998. From 2009 to 2010, he joined professor Jiansheng Dai's group as a Visiting Scholar with the Centre for Robotics Research, King's College London, University of London, London, U.K. He is currently a professor with the School of Mechanical Eng-ineering, Guangxi University. He is the author of three books, more than 150 articles, and more than 170 inventions. His research interests include theory of mechanism and machine, and mechanical dynamics, and nonlinear vibration theory.

JUNJIE GONG was born in 1995. He received the B.S. degree in mechanical manufacturing and its automation from wuhan polytechnic university, Wuhan, China, in 2018. He is currently pursuing the Ph.D. degree with Guangxi University, China. His research interests include mechanical innovation design, and industrial robot, and nolinear vibrations, and mechanical dynamics.

SIXU PENG was born in 1995. She received the B.S. degree from the Shenyang Ligong University, China, in 2017. She is currently pursuing the M.S. degree with Guangxi University. Her research interests include robotic mechanisms, and mechanical dynamics, and nolinear vibrations.